Machine learning for metallurgy V: A neural-network potential for zirconium

Manura Liyanage [1,*] David Reith [2] Volker Eyert [2] and W. A. Curtin [1]

[1] *Laboratory for Multiscale Mechanics Modelling, École Polytechnique Fédérale de Lausanne, CH-1015 Lausanne, Switzerland*

[2] *Materials Design SARL, 42 avenue Verdier, 92120 Montrouge, France*

(Received 27 February 2022; accepted 31 May 2022; published 24 June 2022)

The mechanical performance—including deformation, fracture and radiation damage—of zirconium is determined at the atomic scale. With Zr and its alloys extensively used in the nuclear industry, understanding that atomic scale behavior is crucial. The defects controlling that performance are at size scales far larger than accessible by first principles methods, necessitating the use of semiempirical interatomic potentials. Existing potentials for Zr are not sufficiently quantitative, nor easily extendable to alloys, oxides, or hydrides. To overcome these issues, a neural network machine learning potential (NNP) is developed here within the Behler-Parrinello framework for Zr. With a careful choice of descriptors of the atomic environments and the creation of a first-principles training dataset that includes a wide spectrum of configurations of metallurgical relevance, a very accurate NNP is demonstrated. Specifically, the Zr NNP yields a good description of dislocation structures and their relative energies and fracture behavior, along with bulk, surface, and point-defect properties and structures, and significantly outperforms the best available traditional potentials. Results here will enable large-scale simulations of complex processes and provide the basis for future extensions to alloys, oxides, and hydrides.

DOI: 10.1103/PhysRevMaterials.6.063804

I. INTRODUCTION

The physical properties of zirconium alloys, such as a low neutron absorption cross section accompanied by good mechanical properties and corrosion resistance, [1–4] preordain their usage in nuclear reactors. For instance, they are utilized as fuel cladding, pressure tubes, fuel channels, and fuel spacer grids [5–7]. Zr exhibits a number of complex features relevant to these applications, such as competing slip systems for dislocation motion, multiple possible cleavage planes, several modes of twinning deformations, and a high-temperature hexagonal close-packed (hcp) to body-centered cubic (bcc) phase transformation [4,8–10]. Experimental investigations provide important information about the real material behavior but probing the underlying mechanisms governing the atomic-scale phenomena is challenging. Computational studies provide means for a more in-depth understanding of atomistic mechanisms involved.

First-principles methods such as density functional theory (DFT) provide highly accurate energy information, but the complexity and size of structures that can be analyzed is limited by the high computational cost. Semiempirical potentials using the embedded atom model (EAM) and the modified embedded atom model (MEAM) have been developed to overcome the computational cost [11–13] but with compromises to the accuracy of describing the potential energy surface (PES) leading to lower chemical accuracy and thus reducing the scope of applications. The limited flexibility of these semiempirical potentials for capturing increasingly complex structures, and especially for extensions to alloys, motivates the continued search for more accurate but computationally accessible methods.

The challenges in modeling the mechanical behavior of hcp metals like Zr, Ti, and Mg lie in the diversity of active slip systems and possible fracture modes. Figure 1 shows the accessible active slip systems in hcp Zr. Slip by the $\langle \mathbf{a} \rangle$ Burgers vector has a competition between basal, prismatic I-w, and pyramidal I-n slip planes ("w" represents the wide or loosely packed planes, while "n" represents the narrow or densely packed planes; see Yin *et al.* [14]) since the $\langle \mathbf{a} \rangle$ vector is contained in all three planes. Zr exhibits preferential $\langle \mathbf{a} \rangle$ prismatic I-w slip with some activity on the pyramidal I-n plane due to cross-slip, but with the basal $\langle \mathbf{a} \rangle$ being unstable [15,16]. In contrast, Mg shows preferential basal $\langle \mathbf{a} \rangle$ slip, no pyramidal I $\langle \mathbf{a} \rangle$ slip, and some prismatic activity due to cross-slip. Zr also strongly prefers $\langle \mathbf{c} + \mathbf{a} \rangle$ slip on the pyramidal I-w plane over the pyramidal II plane, whereas in Mg the two slip systems are very similar [17–19]. Due to the high stresses needed to activate $\langle \mathbf{c} + \mathbf{a} \rangle$ slip with deformation in the $\langle \mathbf{c} \rangle$ direction, deformation twinning becomes operative in Zr (and other hcp metals) to provide further $\langle \mathbf{c} \rangle$ axis deformation. High twinning activity has been observed in Zr compared to less ductile hcp metals such as Mg [20]. Fracture behavior involves the surface energies of all of these different possible cleavage planes and the blunting of cracks by dislocation emission on the various slip planes that intersect the crack front. These points highlight that any potential for Zr should accurately capture the competing slip activity and surface energies in Zr.

To address the challenge of modeling Zr a number of EAM and MEAM potentials have been developed by Igarashi *et al.* [21], Ackland *et al.* [22], Pasianot and Monti [23],

*pandula.liyanage@epfl.ch

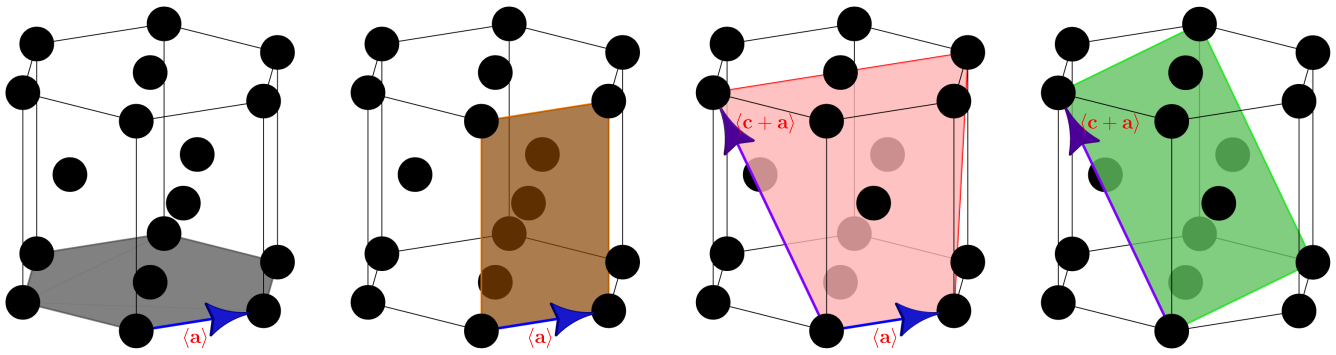

(a) Basal (b) Prismatic I (c) Pyramidal I (d) Pyramidal II

FIG. 1. Slip planes in the hcp crystal structure, where $\langle \mathbf{a} \rangle$ and $\langle \mathbf{c} + \mathbf{a} \rangle$ represent the $1/3\langle 1\bar{2}10 \rangle$ and $1/3\langle 1\bar{2}13 \rangle$ families of dislocations. Basal, prismatic I, pyramidal I, and pyramidal II are the $\{0001\}$, $\{10\bar{1}0\}$, $\{10\bar{1}1\}$, and $\{11\bar{2}1\}$ families of planes, respectively.

and Kim *et al.* [24], achieving varying accuracy for properties such as lattice parameters and elastic constants. The generalized stacking fault energies (GSFEs) that are important for dislocation and fracture behavior are, however, not sufficiently accurate. Wimmer *et al.* [25] recently introduced an EAM potential for Zr-H that describes some important hydride and Zr-H properties well compared to DFT, but the totality of properties of pure Zr studied are not captured with the necessary accuracy. The most widely used Zr potential is that of Mendelev and Ackland [4] that was initially developed to model phase transformations. The Mendelev and Ackland [4] "no. 3" potential was developed for hcp-Zr and predicts many mechanical properties with good accuracy and give reasonable qualitative results for some nonlinear behavior [15,16]. Not surprisingly, due to the limited flexiblity of the EAM form, this potential is inaccurate for a number of slip-related quantities such as the stable stacking fault energy in the prismatic I-w plane $\{10\bar{1}0\}$ that is a critical property for $\langle \mathbf{a} \rangle$ dislocation slip. Thus, at present, there are no comprehensive potentials for Zr that capture the myriad aspects that are necessary for modeling of Zr deformation and fracture.

A new approach to achieving both accuracy and efficiency is through potentials developed using machine learning (ML) techniques. ML methods have the advantage of not being limited to a specific functional form, giving them the ability to be fitted to an *ab initio* PES covering a wide range of the configurational space. Unlike empirical potentials, ML potentials are fitted to local atomic environments rather than properties of materials, and so accuracy depends on sufficient precision and breadth of the structural space to which the ML is applied. Structures should be selected to encompass the metallurgical configurations pertinent to the performance of the potential. The use of *ab initio* methods such as DFT provides the chemical accuracy for the chosen structures. Finally, the adroit choice of local descriptors for representing the local atomic environments and connecting local environments to structure energies provides the computational efficiency, relative to DFT. Hence, the development of a machine learning potential can be divided into the following phases:

(1) Development of a database of structures with *ab initio* calculated energies and forces that accurately capture the PES (forces and energies) relevant to metallurgical properties of interest

(2) Selection of descriptors for the local environments of the chosen structures; these descriptors should be invariant under rotations, translations, and exchange of coordinates of like atoms

(3) Training of an ML potential using the selected descriptors on the database of structures through regression to optimize model parameters that map the descriptors to the local PES

(4) Optimization of the choice of descriptors to enhance efficiency while preserving accuracy of the final potential.

The development of ML potentials for Zr has seen considerable recent success, but with a limited focus on capturing the hcp-bcc phase transition [26–29] and phonon dispersion [30]. ML potentials suitable for modeling of mechanical properties, especially dislocation plasticity and fracture, have not yet been developed. The goal of the present paper is to develop a broadly useful neural network potential (NNP) for Zr that captures the many features important for deformation and fracture of hcp Zr. Current work follows recent developments of NNPs for metals and alloys (Al-Cu [31]; Mg [32]; Al-Mg-Si [33]) using the Behler-Parrinello (BP) framework and symmetry functions (SF) [34,35] as descriptors. The resulting NNP potential captures the mechanical and plastic behavior much better than the best existing EAM potentials.

The remainder of this paper is organized as follows. In Sec. II the methodology of the training process within the BP framework is discussed along with details about the structures included in the training dataset. Section III presents the validation of the developed NNP. Initially, the predictions of energies and the forces of the structures in the dataset are examined in Sec. III A. Then Secs. III B to III F analyze the mechanical and plastic behavior of Zr (lattice parameters, elastic properties, surface energies, stacking fault and decohesion curves, dislocations, twin boundaries, and fracture) observed for "best" NNP potential with comparison to DFT results where available. Comparisons to the Mendelev and Ackland [4] "no. 3" EAM potential will be made for many properties. Section IV summarizes the performance of the NNP for Zr and points toward future work.

II. METHODS

This section summarizes the composition of the training set, the *ab initio* approach applied to the training set to calculate energies and forces, the Behler-Parrinello neural-network potential (NNP) framework, and the selection of symmetry functions (SFs) entering the NNP formalism.

A. Training set

In general, the reference structures used for the training of the neural network should encompass sufficient detail of the atomic environments that are encountered in metallurgical applications. Mechanical, plastic, and fracture properties are the main focus in the current study; we do not attempt to capture the complexities that arise in direct modeling of radiation damage [36,37] The initial training set thus consists of structures relevant for these properties. These include hydrostatically and uniaxially strained structures (within 6% strain of the equilibrium lattice parameters) as well as structures with vacancies and vicinal surfaces of the different crystalline phases of Zr (hcp, fcc, bcc, and hexagonal ω phases). Additionally, snapshots of *ab initio* molecular dynamics simulations at 1000 K of the above-mentioned structures were also considered. Exclusively for the hcp phase, structures related to decohesion curves, generalized stacking fault energy curves, and stable stacking faults along relevant directions of the various active slip planes (see Fig. 1) and self-interstitials are also included in the training set. NNPs trained on this dataset perform sufficiently well for many properties but, similar to the case of Mg [32], perform very poorly in fracture tests. To rectify this problem, guided by previous work on Mg, additional structures consisting of hcp rod and cuboidal structures that contain corners and edges are added to the training set, leading to significant improvement in fracture performance (see Sec. III F). The final total dataset consisted of 1875 structures containing a total of 96 981 atoms that encompass a broad range of local atomic environments.

In the loss function used to create the NNP (see Eq. (7)) the total energy of each structure is considered irrespective of the size of the cell. The number of atoms in all structures of the training set is kept at comparable values in order to avoid bias towards larger structures [32]. Specifically, most structures have between 32 and 72 atoms while the the rod and cuboidal structures have 216 atoms. These system sizes are all large enough to avoid any size effects entering the DFT reference energies and structures.

B. DFT methodology

All training set calculations are based on density functional theory (DFT) [38,39] with electron-electron exchange and correlation effects described within the standard generalized gradient approximation (GGA) as proposed by Perdew *et al.* [40]. The Kohn-Sham equations were solved with projector-augmented-wave (PAW) potentials (PAW_PBE Zr_sv 04Jan2005) and wave functions [41] as implemented in the Vienna Ab initio Simulation Package (VASP version 6.0) [42,43]. Specifically, the basis set comprised the 4*s*, 4*p*, 5*s*, and 4*d* states. The planewave cutoff energy was set to 520 eV, and a Γ-centered Monkhorst-Pack **k**-point mesh with a spacing of 0.2 $Å^{-1}$ [44] was used as well as a Gaussian integration scheme with a broadening of 0.05 eV. All calculations were performed within the MedeA computational environment of Materials Design [45].

For the training data set used here (1875 structures, each containing 20 to 216 atoms), the total energies of these structures cover a wide range between −1840.58 and −168.50 eV. More interesting are the energies per atom, which vary from −8.52 to −7.47 eV/atom. The atomic forces are found between −39.5 and 34.2 eV/Å.

C. Neural-network formulation and symmetry functions

In the same way as classical potentials, machine-learned potentials (MLP) establish the potential energy of a structure as a sum of the individual atom contributions [34,46]. The potential energy E of a structure with N atoms is calculated as

$$E = \sum_{n=1}^{N} E_n, \tag{1}$$

where E_n is the individual atom energy of the nth atom. The atomic energies depend on the local environments around each individual atom and are resolved by means of local descriptors, also called symmetry functions [34,35,46]. Here we use three types of Behler-Parrinello SFs: radial (G^2), narrow angular (G^3), and wide angular (G^9) SFs, having the functional forms

$$G_i^2 = \sum_{i \neq j} e^{-\eta(r_{ij}-r_s)^2} f_c(r_{ij}), \tag{2}$$

$$G_i^3 = 2^{1-\zeta} \sum_{j,k \neq i} (1 + \lambda \cos\theta_{ijk})^{\zeta} e^{-\eta\left(r_{ij}^2 + r_{ik}^2 + r_{jk}^2\right)} \times f_c(r_{ij}) f_c(r_{ik}) f_c(r_{jk}), \tag{3}$$

$$G_i^9 = 2^{1-\zeta} \sum_{j,k \neq i} (1 + \lambda \cos\theta_{ijk})^{\zeta} e^{-\eta\left(r_{ij}^2 + r_{ik}^2\right)} \times f_c(r_{ij}) f_c(r_{ik}), \tag{4}$$

where $r_{ij} = |\mathbf{r_j} - \mathbf{r_i}|$ is the radial distance between atoms i and j and θ_{ijk} the angle between the vectors from atom i to atoms j and k, respectively. While r_{ij} in the Gaussian components of angular SFs (G^3 and G^9) can be shifted by r_s similar to radial SFs, they are generally kept at zero 0, and hence not included in Eqs. (3) and (4). The so-called hyperparameters η and r_s vary the width and radial position of the Gaussian functions in the radial SFs. The cutoff function f_c smoothly decreases the radial components to zero at a radial cutoff r_c (for the current work, $f_c(r) = \tanh^3(1 - r/r_c)$). The hyperparameters λ and ζ define the shape of the angular components of the SFs. For the radial SFs, the hyperparameters are varied in two ways. For shifted SFs ($G^{2,s}$), η is kept constant and r_s is varied, while for centered SFs ($G^{2,c}$), $r_s = 0$ while η is varied. Eqs. 3 and 4 have the same angular variation, while the radial components are different. The choice of the SFs (chosen hyperparameters) needs to be optimized to capture the local atomic environments sufficiently without overfitting and with the fewest number of SFs for the best computational

efficiency. The process of SF selection will be discussed later in this section.

Atom energies are calculated through a neural network with two hidden layers as

$$E_n = f_1^3\Bigg\{b_1^3 + \sum_{k=1}^{M_{\text{layer},2}} w_{k1}^{23} f_k^2 \times \Bigg[b_k^2 + \sum_{j=1}^{M_{\text{layer},1}} w_{jk}^{12} f_j^1\left(b_j^1 + \sum_{i=1}^{M_{\text{sym}}} w_{ij}^{01} G_i\right)\Bigg]\Bigg\}, \quad (5)$$

where $f(\cdot)$ are the activation functions for each node (for the current study f_j and f_k are softplus functions and f_1 is the identity function), $M_{\text{layer},m}$ is the number of nodes in the mth hidden layer, M_{sym} is the number of SFs (G_i). Fitting parameters of the training are the weights and the biases, w_{pq}^{uv} and b_q^v, connecting the pth node in the uth layer or the bias to the qth node in the vth layer, of the neural network. Force components of the nth atom ($F_{n,i}$) are obtained by taking the derivative of the total energy (E) with the spatial coordinate of the atom ($x_{n,i}$) as

$$F_{n,i} = \frac{\partial E}{\partial x_{n,i}} = \sum_{m=1}^{N} \frac{\partial E_m}{\partial x_{n,i}} = \sum_{m=1}^{N}\sum_{j=1}^{M_{\text{sym}}} \frac{\partial E_m}{\partial G_j}\frac{\partial G_j}{\partial x_{n,i}}. \quad (6)$$

Training is carried out through regression to minimize the loss function [47],

$$\Gamma = \sum_{i=1}^{N_{\text{struct}}} \left(E_{\text{NN}}^i - E_{\text{ref}}^i\right)^2 + \beta^2 \sum_{i=1}^{N_{\text{struct}}}\sum_{j=1}^{3N_{\text{atom}}^i} \left(F_{j\text{NN}}^i - F_{j\text{ref}}^i\right)^2, \quad (7)$$

where E and F are the energies of the structures and the forces of the atoms in each of these structures, respectively. β (with Å units) is used to scale the relative weight of the forces (in eV/Å) vs the energies (in eV). Performance of the training is initially assessed with root mean square errors (RMSEs) calculated separately for energy and forces as

$$\text{RMSE}_{\text{E}} = \sqrt{\frac{1}{N_{\text{struct}}}\sum_{i=1}^{N_{\text{struct}}} \left(E_{\text{NN}}^i - E_{\text{ref}}^i\right)^2}, \quad (8)$$

$$\text{RMSE}_{\text{F}} = \sqrt{\frac{1}{N_{\text{struct}}}\sum_{i=1}^{N_{\text{struct}}}\sum_{j=1}^{3N_{\text{atom}}^i} \frac{1}{3N_{\text{atom}}^i}\left(F_{j\text{NN}}^i - F_{j\text{ref}}^i\right)^2} \quad (9)$$

to provide an overall estimate of how well the structures in the dataset are represented by the NNP. Subsequently, the resulting NNP is used to compute bulk, surface, and point defect properties, which enables assessment of the quality of the potential for capturing the key metallurgical features.

The NNP training is carried out using the open source code `n2p2` [48]. Training is performed with a Kalman filter for a fixed number of 400 epochs, as proposed by Stricker *et al.* [32]. All structures in the dataset are used for training since validation of the NNP will eventually rest on computed properties, not direct comparison of the NNP to the training data. Initially $\beta = 10$ Å was used for the force weighting in Eq. (7), as used in Stricker *et al.* [32], but greatly improved training quality was achieved using $\beta = 1$ Å. Also at each epoch, only 2% of the forces (selected randomly from candidates whose current error falls above a certain threshold) and 100% of the energies of the training dataset are updated. Larger values of the fraction of force used led to much larger RSMEs.

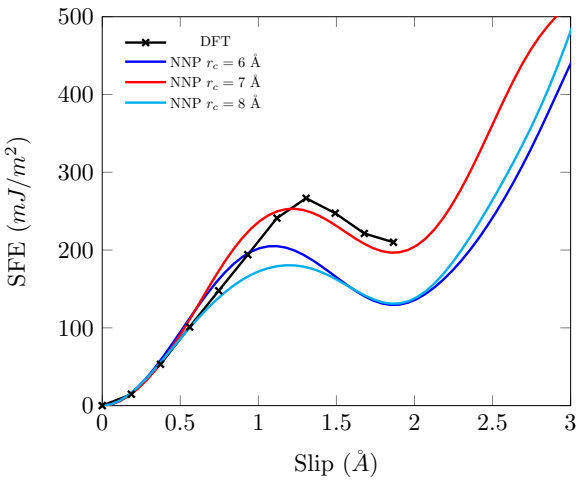

FIG. 2. Generalized stacking fault energy.

D. Selection of symmetry functions

Selection of SFs is crucial in developing an accurate and efficient NNP. The final SFs here are chosen after a number of trials by investigating the predicted bulk, surface, and point-defect Zr properties. To describe a single set of SFs, the format "$\mu r_c, iG^{2,s}, jG^{2,c}, lG^3, kG^9$" is used, where μ, i, j, k, and l indicate the radial cutoff (r_c) and the number of $G^{2,s}$, $G^{2,c}$, G^3, and G^9 SFs, respectively. For each set of SFs, training is done for 10 different random initial sets of weights and biases. Zr has a c/a ratio which is quite low compared to the ideal c/a ratio, indicative of angular bonding in such hcp structures and thus suggesting the need for additional angular symmetry functions to describe the local environments.

The initial set of SFs follows Stricker *et al.* [32], who successfully developed an NNP for hcp Mg. This set contains 82 unique SFs, with 32 radial SFs and 50 narrow angular SFs as shown in Eqs. (2) and (3), has r_c of 6, 8, 9, and 12 Å for the radial SFs, and 6 and 12 Å for the narrow angular SFs. SF hyperparameters are selected as guided by Imbalzano *et al.* [49], with no wide angular SFs. Thereafter the number of SFs is reduced using a CUR decomposition algorithm [49] to obtain the 48 most useful SFs. Training with these SFs yields an NNP of poor quality, with RMSEs of ∼20 meV/atom and ∼150 meV/Å for energy and forces, respectively. This indicates that this initial set of SFs is unsuitable for capturing the atomic environments that control energies and forces in Zr. Hence, a new set of SFs is selected with a single radial cutoff of 6 Å containing 66 unique SFs ($6r_c, 10G^{2,s}, 8G^{2,c}, 24G^3, 24G^9$) including now the wide angular SFs, where the hyperparameters of the shifted angular SFs is determined on a grid as proposed by Gastegger *et al.* [50] and the hyperparameters of the remaining SFs selected as per Imbalzano *et al.* [49]. Again the CUR selection algorithm is used to find the 48 "best" SFs. The NNP

$r_c = 6$ Å

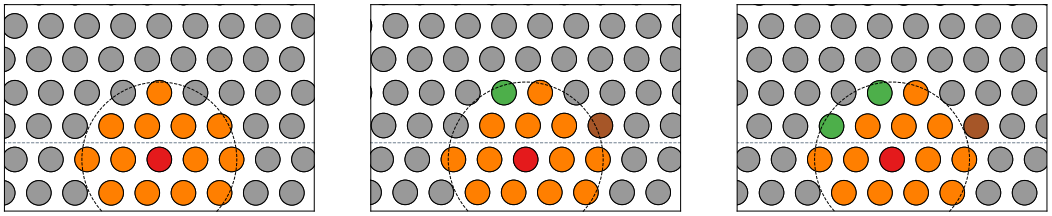

(a) Equilibrium position (b) Unstable stacking fault (c) Stable stacking fault

$r_c = 7$ Å

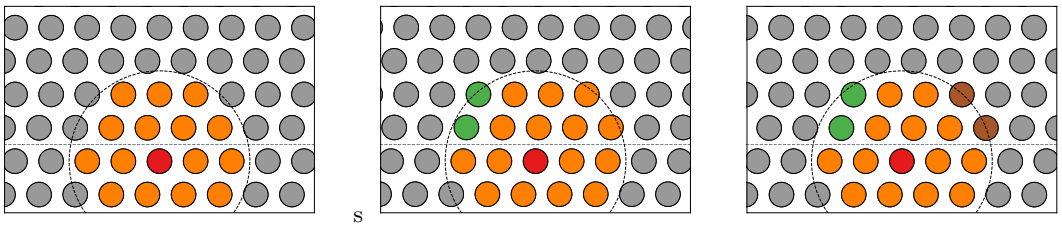

(d) Equilibrium position (e) Unstable stacking fault (f) Stable stacking fault

$r_c = 8$ Å

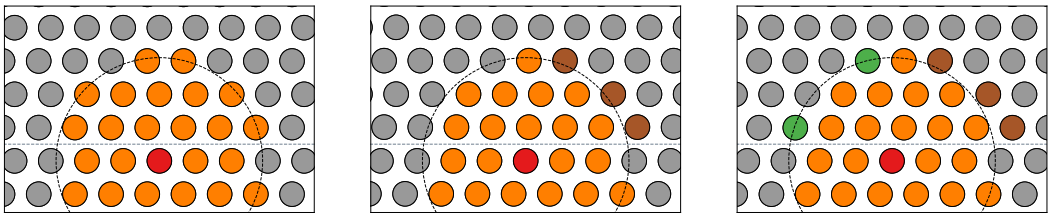

(g) Equilibrium position (h) Unstable stacking fault (i) Stable stacking fault

FIG. 3. Atoms above the basal slip plane lying within the radial cutoff distance of an atom just below the slip plane for different radial cutoff (r_c) values. The central atom below the slip plane is shown in red, while the atoms entering the r_c are shown in the green, atoms leaving the r_c are shown in brown, atoms remaining inside r_c are shown in orange, and all other atoms are shown in gray. The dotted lines indicate the slip plane.

developed with this set of SFs resulted in significant improvements, with reductions in the RMSEs of energy and force to 4–6 meV/atom and 80–100 meV/Å, respectively.

With the above encouraging results, a broader sensitivity analysis is executed considering combinations of radial cutoffs of 6 Å, 8 Å, 10 Å, 6+8 Å, and 6+8+10 Å. Using the CUR selection algorithm, the 48 "optimal" SFs were selected for each case. The best RMSE values were obtained using the combination of 6+8 Å radial cutoffs. Although improvement is observed with RMSE ($\mathrm{RMSE_E} \approx 4$ meV/atom and $\mathrm{RMSE_F} \approx 80$ meV/Å), the stacking fault curves are faulty, with the unstable basal stacking fault energies significantly lower than the DFT values. It was speculated that this could be due to the radial cutoff, since a stacking fault will incur a large displacement along the plane, which can cause notable changes to the atomic environment within any given radius.

Hence, the analysis for the sensitivity to the radial cutoff was extended to the SF sets of the following:

(1) 6 Å ($6r_c$, $11G^{2,s}$, $6G^{2,c}$, $48G^3$, $48G^9$)
(2) 7 Å ($7r_c$, $13G^{2,s}$, $6G^{2,c}$, $48G^3$, $48G^9$)
(3) 8 Å ($8r_c$, $15G^{2,s}$, $6G^{2,c}$, $48G^3$, $48G^9$)
(4) 9 Å ($9r_c$, $17G^{2,s}$, $6G^{2,c}$, $48G^3$, $48G^9$).

The number of most useful SFs selected by CUR decomposition method is also varied to find the number of SFs required to accurately represent atomic environments. From these, the NNPs developed with a radial cutoff of 7 Å and 80 SFs showed the best RMSE and the deviations in the generalized stacking fault curves decreased significantly (see below).

Identifying that the radial cutoff r_c for the symmetry functions must be set to 7 Å for good accuracy is one main breakthrough in achieving a very good overall NNP for Zr; Fig. 2 shows the predicted basal GSFEs for $r_c = 6$, 7, and 8 Å where the most significant improvement was found. Thus atomic positions relative to the r_c during basal slip are examined. Focusing on an atom just below the slip plane, the atoms above the slip plane within r_c are shown in Fig. 3 for the perfect crystal, the unstable stacking fault configuration, and the stable stacking fault configuration. For $r_c = 6$ Å, only a few atoms in the first two planes above the slip plane interact with the lower atom, and various atoms are entering and exiting the

domain within the cutoff. For $r_c = 7$ Å, several atoms enter the domain at the unstable point and then exit the domain at the stable fault, but in a smooth manner relative to the situation for $r_c = 6$ Å. For $r_c = 8$ Å, overall more atoms are included, naturally, but there are significant shifts of atoms out of the domain without rather different atoms entering the domain. It may be that the relatively symmetric case for $r_c = 7$ Å avoids small changes in total energy that may occur in the asymmetric cases of $r_c = 6$ and 8 Å that, while small, are fully attributed to the (also small) GSFE energy changes and thus may lead to inaccurate stacking fault results. This examination is far from rigorous, but suggests why a particular cutoff of $r_c = 7$ Å may be notably better than other choices.

Based on the above studies, a set of ten NNPs with different initial weights and biases were developed using the final set of SFs (80 SFs chosen with CUR selection from $7r_c$, $13G^{2,s}$, $6G^{2,c}$, $48G^3$, $48G^9$). As shown in the next section, these NNPs have low RMSE for the forces and energies of structures in the training dataset, and will subsequently be shown to give good bulk and defect properties, relative to DFT. Comparisons to results from one EAM potential (Mendelev and Ackland [4] "no. 3" potential) will also be shown.

III. RESULTS AND DISCUSSION

To evaluate the quality and the usefulness of a potential for metallurgical problems an examination of its application on various properties is required. A comprehensive investigation is performed considering mechanical and elastic properties, surface energies and decohesion curves, stacking fault curves, dislocation core structures, twin boundaries, and fracture behavior. Each of these aspects are discussed below in detail. The same properties are also investigated with an EAM potential (Mendelev and Ackland [4] "no. 3" potential) and are discussed briefly for comparison. All the predicted properties are obtained through simulations performed with `LAMMPS` [51] with the `n2p2` module for the NNPs and using system sizes equal to and larger than those used for the DFT training data with no dependence of properties on system size. `Ovito` is used in visualizing the atomic structures [52].

A. NNP energies and forces vs DFT reference values

The 10 NNPs developed with the final set of symmetry functions give similar RMSE ($\text{RMSE}_\text{E} < 1$ meV/atom and $\text{RMSE}_\text{F} \approx 60$ meV/Å). To select the most balanced NNP from among the 10 NNPs, a root mean square percentage error (RMPSE) is calculated as

$$\text{RMPSE} = \sqrt{\frac{1}{N}\sum_{i=1}^{N}\left(\frac{\text{X}_\text{NNP} - \text{X}_\text{DFT}}{\text{X}_\text{DFT}}\right)^2} \times 100, \qquad (10)$$

with $X = 1, \ldots, N$ being the elastic properties (the five independent components for hcp crystals (C_{11}, C_{12}, C_{13}, C_{33}, C_{44}) and the stacking fault energies (unstable (γ_usf) and lower (γ_lsf, which may be different from the stable stacking fault energy) defined as the first maxima and the first minima of the GSFE curves) for basal {0001}, prismatic I-w $\{10\bar{1}0\}$, pyramidal I-w $\{10\bar{1}1\}$, and pyramidal II $\{11\bar{2}1\}$ planes (see Fig. 1) with $N = 13$. The NNP denoted "NNP4" is found to give the best RMPSE of 7.33%, along with best agreement for most individual properties, with other NNPs having RMPSEs between 10% and 16%. NNP also has errors of $\text{RMSE}_\text{E} = 0.712$ meV/atom and $\text{RMSE}_\text{F} = 60.58$ meV/Å relative to the DFT training set. Finally, NNP4 is also found to perform well for dislocation, twin boundaries, and fracture simulations (see below). Hence, NNP4 is selected as the proposed NNP emerging from the current study that is capable of modeling most mechanical and plastic behavior of Zr with very good agreement to DFT results and other *ab initio* studies available in the literature. The SFs and the respective hyperparameters of NNP4 are shown in the Appendix.

The energies and forces predicted by NNP4 follows the trend of the reference values with no discernible outliers. Figure 4(a) shows a histogram of percentage errors of NNP4 energies relative to the DFT database. The majority of the energy errors (∼90%) are below 1 meV/atom, which is comparable to DFT accuracy. No errors are above 10 meV/atom, which is excellent. On the other hand, Fig. 4(b) shows a histogram of percent forces errors, which are much larger. The maximum error of 1.76 eV/Å is found for a structure having a self-interstitial and most of the large errors (>500 meV/Å) were also for similar structures containing self-interstitials (minimum energy structure and snapshots of the molecular dynamic evolution of this structure at 1000 K), but the DFT forces of these structures were immense (7 to 30 eV/Å) and hence the relative errors are between 5% and 20% and these structures will rarely occur in reality. The high error could be due to the fact that there are only a small number of atomic environments in the training set that come close to these interstitial configurations, causing less accurate PES and then large force errors (derivatives of the PES). Although these force errors are quite significant, the equilibrium Zr self-interstitial energy and the atomic configuration predicted by NNP4 are in good agreement with the DFT values.

B. Lattice, elastic, and surface properties

A summary of properties commonly used to compare interatomic potentials is shown in Table I as calculated via DFT, NNP4, and the Mendelev and Ackland [4] "no. 3" EAM potential. Figure 5 shows the percentage errors of these properties relative to DFT. Overall, there is very good agreement between NNP4 and DFT, with almost every property of NNP4 captured more accurately than that of the EAM, which was often fitted directly to the properties (although not to the precise DFT executed here).

A closer look at the lattice parameters from both potentials (EAM and NNP) show that they match DFT well, which itself slightly overestimates experimental values. The c/a ratio for Zr is quite low compared to the ideal value for hcp structures of $\sqrt{8/3}(\approx 1.633)$. This difference may account for the substantially greater difficulty in obtaining a good NNP for Zr as compared to earlier studies for near-ideal-c/a Mg, necessitating the use of many more SFs (with higher number of angular symmetry functions) and inclusion of the wide-angle SFs.

TABLE I. Comparison of the properties obtained for the NNP4 with the corresponding properties obtained from DFT calculations and the EAM (Mendelev and Ackland [4] "no. 3") potential. Between the EAM and NNP4, the most accurate prediction for each property (compared to DFT values) are shown in bold.

Property	Experimental	DFT (0 K)	NNP4	EAM
Lattice parameters				
a (Å)	3.228[a]	3.237	3.231	3.234
c/a	1.592[a]	1.595	1.602	1.598
Elastic properties (GPa)				
C_{11}	155[b]	150	**141.5**	**141.5**
C_{12}	67[b]	61	**67.2**	74.2
C_{13}	65[b]	66	**67.2**	74.0
C_{33}	173[b]	153	**168.7**	**167.7**
C_{44}	36[b]	31	**28.9**	43.9
Surface energies (mJ/m^2)				
γ_{surf}: basal	—	1580	**1593.8**	1528.9
γ_{surf}: prismatic I-w	—	1664	**1631.9**	1540.8
γ_{surf}: pyramidal I-w	—	1573	**1582.9**	1553.8
γ_{surf}: pyramidal II	—	1713	**1731.1**	1645.4
Stacking fault energies (mJ/m^2)				
γ_{lsf}: basal	—	215	**196.7**	**197.8**
γ_{lsf}: prismatic I-w	—	208	**219.7**	135.5[c]
γ_{lsf}: pyramidal I-w	—	202	**198.6**	161.8
γ_{lsf}: pyramidal II	—	399	**400.8**	339.2
γ_{usf}: basal	—	271	**253.1**	323.4
γ_{usf}: prismatic I-w	—	223	**237.0**	272.7
γ_{usf}: pyramidal I-w	—	482	**461.1**	336.1
γ_{usf}: pyramidal II	—	580	**545.8**	415.2
γ_{ssf}: pyramidal I-w	—	113	**139.2**	**136.1**
γ_{ssf}: pyramidal I-n	—	161[d]	**164.0**	244.2
γ_{ssf}: pyramidal II	—	304	**290.9**	334.8
Other properties				
Vacancy formation energy E_{vac} (eV)	—	2.02	**2.04**	1.69
Self-interstitial energy E_{SIA} (eV)	—	2.99	**3.01**	2.77
$E_{bcc-hcp}$ (eV)	—	0.084	**0.085**	0.103
$E_{fcc-hcp}$ (eV)	—	0.038	**0.037**	0.054

[a]Goldak *et al.* [53] at 0 K.
[b]Fisher and Renken [54] at 4 K.
[c]For prismatic I-w plane, the generalized stacking fault energy curve doesn't show a minimum. The value here indicates the stable stacking fault energy only obtained with an additional 0.15c [0001] shift from the expected minimum. Ref. [54] confirms this.
[d]Yin *et al.* [14].

The 10 NNPs based on the final set of symmetry functions yield elastic properties that are in fair agreement with DFT values. In general large variations are observed for C_{12} and C_{13}, but NNP4 gives very good agreement for C_{12} and C_{13} (see Fig. 5). The predicted C_{33} is overestimated by all the NNPs but coincidentally these are closer to the experimental value. Overall for elastic properties, NNP4 shows the best agreement but the EAM potential is on par with most of the NNPs. It is noted that DFT itself differs from experiments, underestimating C_{33} and C_{44} (as reported also in [55–59]).

The equations of states (EOS) for hcp and bcc Zr as predicted by the NNP and the EAM are compared to DFT result (Fig. 6). The DFT structures in the training dataset are only in the range of ±6%, and here the NNP and EAM both agree well with DFT. Both EAM and NNP4 deviate from DFT for $a/a_0 < 0.9$ and $a/a_0 < 0.94$ for hcp and bcc phases respectively, but the EAM result is smooth, by construction, whereas NNP4 becomes highly unphysical at very large compression. This domain is not relevant for most metallurgical problems, but can be important in studying radiation damage phenomena. The erroneous behavior under high compression can be rectified by the addition of a simple cut-and-shifted Lennard-Jones (LJ) pair potential at small atom separations (see, for example, Jain *et al.* [33]). Figure 6 shows the total potential using the LJ parameters $\epsilon = 5$ eV and $\sigma = 2.584$ Å with cutoff at $r_c = 2^{1/6}\sigma = 2.90$ Å; while the high-compression regime does not match DFT, it avoids the unphysical behaviors and is in an energy range that is not relevant for most applications. Similar results are obtained for the $T = 0$ K EOS of bcc Zr using the same LJ parameters. The only property value shown in Table I that is affected by introduction of the cut-and-shifted LJ potential is the self-interstitial energy, which is increased by 0.2 eV.

Surface energies predicted by the NNPs are in excellent agreement with the DFT results across all the different vicinal surfaces studied (Table I). The decohesion behavior, i.e., rigid

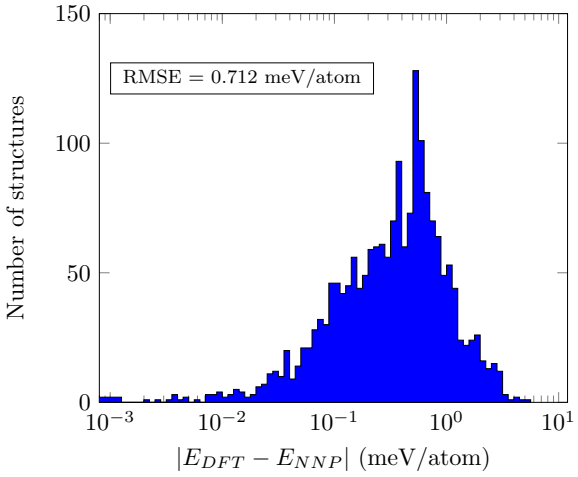

(a) Errors in energy

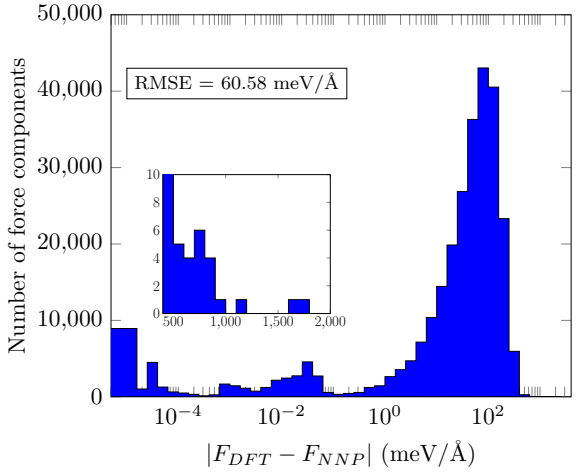

(b) Error in forces

FIG. 4. Histogram of errors for energies and forces of the structures in the dataset as predicted by NNP4. The tiny fraction of structures having force errors >500 meV/Å (see text for discussion) are shown in the inset.

separation of two semi-infinite blocks of perfect crystal normal to the surface of interest, is also very well captured by the NNPs for all surfaces studied (see Fig. 7). Surface energies are often a source of larger error for many available Zr potentials (e.g., Wimmer *et al.* [25], Kim *et al.* [24] with errors of ∼25%). The Mendelev and Ackland [4] "no. 3" EAM shows fair agreement with DFT, but the decohesion behavior is not as well described, but mainly at larger separation distances. The decohesion behavior provides the base-level behavior associated with atomic-scale separation at a sharp crack tip, and the relaxed surface energy sets the load level for cleavage fracture. It is necessary, but not sufficient, for both of these features to be well reproduced for applications of any potential to fracture problems.

C. Stacking fault energies

The generalized stacking fault energies (GSFEs) of all the different slip planes are very important in predicting the plasticity behavior as they significantly influence the dislocation core structures and energies, and the often delicate energetic competition between slip modes. DFT calculated stacking fault curves and fully relaxed stable stacking fault energies (SSFEs) agree well with results from Yin *et al.* [14]. These are included in the training dataset. Since the basal, prismatic I-wide, and pyramidal I-narrow slip planes (see Yin *et al.* [14]) all contain the critical ⟨**a**⟩ screw dislocation while the pyramidal I-w and pyramidal II planes both contain the ⟨**c** + **a**⟩ screw dislocation (see Fig. 1), careful determination of the stacking fault energies for these planes is especially important in Zr.

Figure 8 shows the GSFE curves along the basal, prismatic I-w, pyramidal I-w, and pyramidal II directions obtained from DFT calculations, the NNPs, and the EAM potential. The fully relaxed stable stacking fault energies are also shown with an ∗. It is important to note that the stable stacking fault energies in the pyramidal I-w, pyramidal I-n, and pyramidal II planes deviate significantly from the minima of the GSFE curves due to nonnegligible atomic relaxations of atoms not immediately adjacent to the slip plane (again see Yin *et al.* [14]). The NNPs show quite good agreement for most of the crucial details in the GSFE (see Table I and Fig. 8), while the EAM potential studied here, and all others investigated, show very poor stacking fault energies. Similar to the elastic properties, among the NNPs, NNP4 gives the overall best agreement with the DFT results.

Looking in detail, the NNP predictions for the prismatic I-w slip show some variability. However, all NNPs predict a local minimum (stable stacking fault). The existence of this minimum is quite important since it indicates that a stable ⟨**a**⟩ screw dislocation can exist on this plane, and experimentally this is the dominant ⟨**a**⟩ slip plane in hcp Zr. This differs significantly from hcp Mg, for example, where the prismatic I-w has no local minimum and the ⟨**a**⟩ is not stable relative to the basal ⟨**a**⟩ [32]. The actual dislocations will be analyzed later.

In addition, the pyramidal I-w stable stacking fault is substantially lower than that on the pyramidal II plane. This indicates that the pyramidal I-w ⟨**c** + **a**⟩ is strongly preferentially relative to the pyramidal II ⟨**c** + **a**⟩, and indeed pyramidal I-w slip is observed in Zr and pyramidal II slip is essentially absent. Again, this contrasts with Mg, where the two fault energies are almost equal, and pyramidal II slip is very slightly favorable relative to pyramidal I-w slip, as observed experimentally.

Mendelev and Ackland [4] only considered the SSFE in the basal and prismatic I-w planes when developing the EAM potential (Mendelev and Ackland [4] "no. 3") for the stacking fault energies due to the limited form of the potential. Hence, important aspects of the GSFE curves may not be accurately captured. As observed in Fig. 8(a), the SSFE in the basal plane is determined accurately with the EAM potential but the SSFE in the prismatic I-w plane shows a considerably lower energy (135.5 mJ/m^2) than the DFT value, and also with an offset of 0.15c[0001] from the path of the GSFE curve. Udagawa *et al.* [60] found that the reason for the incorrect SSFE in the prismatic I-w plane was the use of an incorrect DFT reference value (145 mJ/m^2 as given by Domain *et al.* [61]) due to an insufficient number of planes in the simulation cell.

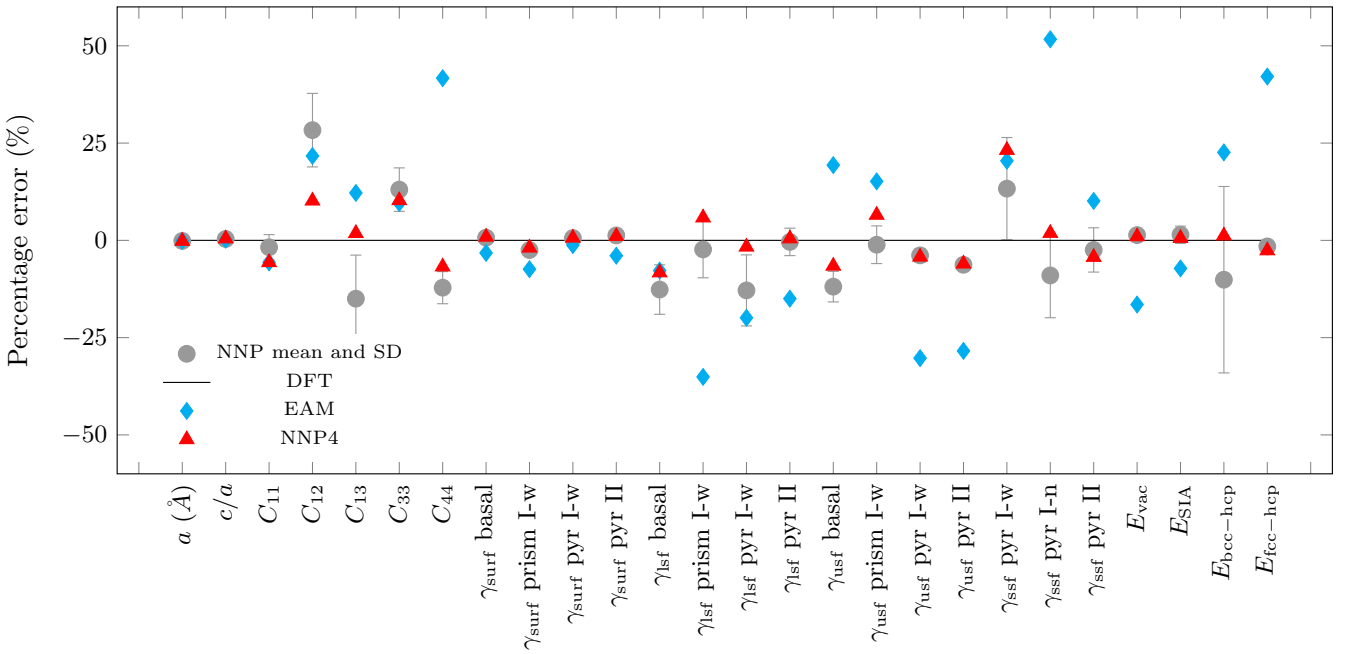

FIG. 5. Percentages errors compared to DFT for the material properties shown in Table I. EAM refers to the Mendelev and Ackland [4] "no. 3" potential. For the mean and standard deviation (SD) the 10 NNPs developed with the final set of symmetry functions are considered.

Bacon and Vitek [62] also showed that potentials with simple hard-sphere models, such as EAMs, inherently suffer from an artifact for the hcp structures wherein the stable stacking fault position for the prismatic I-w plane is found with an offset of $\alpha c[0001](\alpha \neq 0)$ from the GSFE path. Thus, the SSFEs for the pyramidal planes (pyramidal I-w and pyramidal II) are at incorrect positions even though the SSFE values show some agreement with DFT. The EAM fails to capture remaining aspects of the GSFE curves such as the unstable stacking fault energy, which is expected because such information is not included in the fitting process.

D. Dislocations

The plastic flow of metals mainly depends on the availability and mobility of dislocations. Hence, accurate descriptions of all the dislocation core structures are quite important. With the hcp crystal structure, the relevant dislocations are those with Burgers vectors $\langle \mathbf{a} \rangle$ ($\frac{1}{3}\langle 1\bar{2}10 \rangle$) and $\langle \mathbf{c}+\mathbf{a} \rangle$ ($\frac{1}{3}\langle 1\bar{2}13 \rangle$) (Fig. 1). $\langle \mathbf{a} \rangle$ dislocations are dominant, but c-axis deformation, required to satisfy the von Mises criterion for macroscopic plasticity, necessitates the motion of $\langle \mathbf{c}+\mathbf{a} \rangle$ dislocations or twinning. The five possible glide planes are the basal, prismatic I-w, and pyramidal I-n for $\langle \mathbf{a} \rangle$ dislocations and

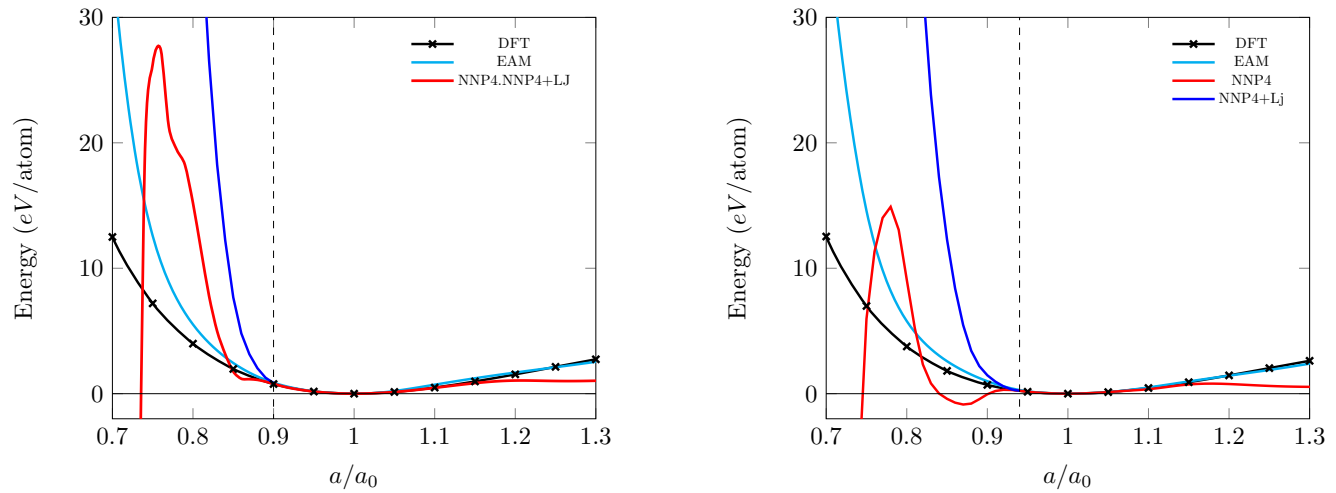

(a) hcp (b) bcc

FIG. 6. Equation of state for Zr obtained with DFT, EAM (Mendelev and Ackland "no. 3" potential), and NNP4 for (a) hcp and (b) bcc structures. NNP4+LJ shows the modified EOS using the NNP4 and a cut-and-shift LJ potential to avoid unphysical behavior for high compressive strains.

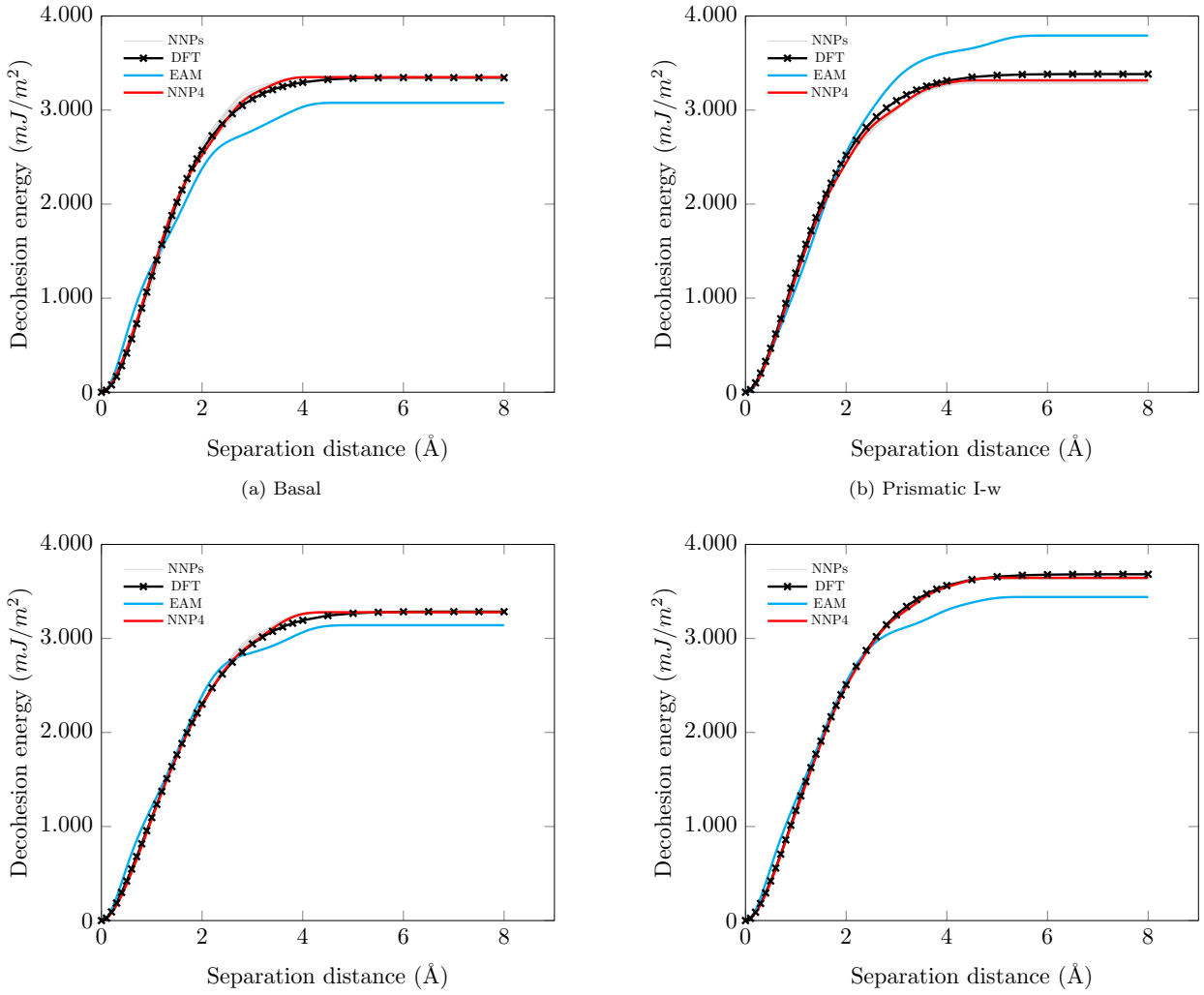

(a) Basal

(b) Prismatic I-w

(c) Pyramidal I-w

(d) Pyramidal II

FIG. 7. Decohesion curves for basal, prismatic I-2, pyramidal I-w, and pyramidal II planes, comparing the DFT, EAM (Mendelev and Ackland [4] "no. 3" potential), and the 10 NNPs developed with the final set of symmetry functions. NNP4 is shown in red to distinguish it from rest of the NNPs. All initial structures here are contained in the training dataset, with the non-DFT results corresponding to relaxed structures using the relevant potential.

pyramidal I-w and pyramidal II for $\langle \mathbf{c} + \mathbf{a} \rangle$ dislocations, as shown in Fig. 1.

Here all five slip systems are analyzed for the relevant edge and screw dislocations separately (10 different core structures). For each case, initial full dislocation and expected partial dislocations are created using the anisotropic Volterra elastic dislocation solution [63], with initial partial dislocation spacings ranging from 5 to 30 Å in steps of 5 Å along the respective slip planes. Simulation cells with in-plane dimensions of approximately 300 Å × 300 Å with one periodic length along the dislocation line direction are used. During relaxation starting from the initial structure, the outer boundary atoms in a 10 Å-thick layer are fixed and all inner atoms are relaxed until a stable configuration is reached. The resulting dislocation core structures are analyzed using the Nye tensor [64,65], differential displacement maps [66], and disregistry along the slip plane using the `atomman python` package [67]. Gradients of the disregistries give the Burgers vector distribution along the glide plane and enable an estimate of any dissociation into partial dislocations [68].

Edge dislocations are stable for all these slip planes but the same screw dislocation can exist on several different planes. Hence, the energetic competition among the different slip systems for the same Burgers vector screw dislocation is crucial to the deformation. The stability of a screw dislocation on a given plane is mainly determined by the stacking fault energy, and it is encouraging that NNP4 captures these energies with good accuracy.

For the critical $\langle \mathbf{a} \rangle$ screw dislocation, previous computational studies [15,16,69] and experimental investigations [70,71] find that the most stable $\langle \mathbf{a} \rangle$ screw dislocation plane in Zr is the prismatic I-w plane. DFT studies using periodic systems with dislocation dipoles in relatively small simulation cells have predicted metastable pyramidal I-n core structures that have higher energies (per dislocation line length) of 3.2 ± 1.6 meV/Å [16] and ∼2.9 meV/Å [72],

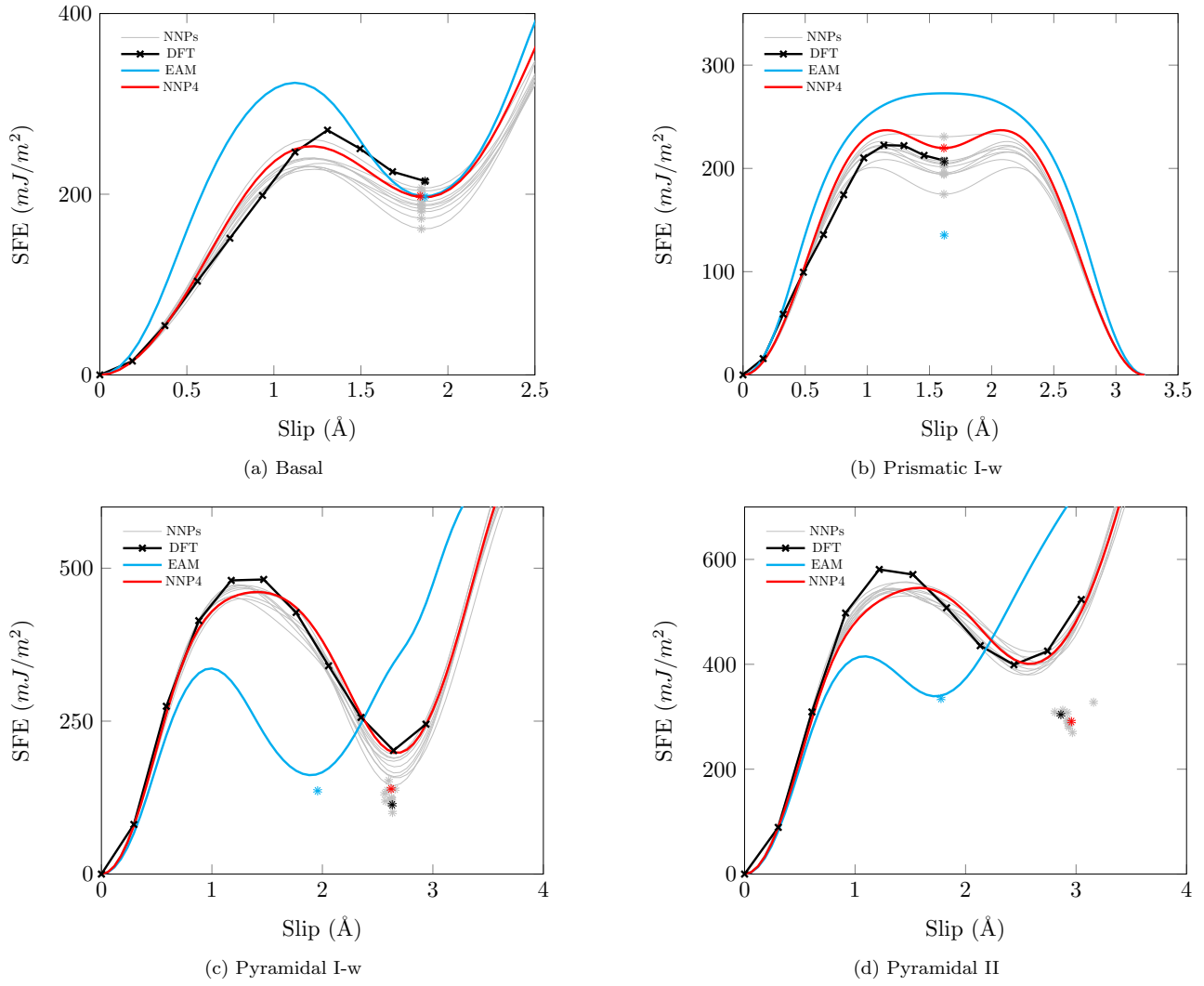

(a) Basal (b) Prismatic I-w

(c) Pyramidal I-w (d) Pyramidal II

FIG. 8. Generalized stacking fault energy curves for basal, prismatic I-2, pyramidal I-w, and pyramidal II planes, comparing the DFT, EAM (Mendelev and Ackland [4] "no. 3" potential), and the 10 NNPs developed with the final set of symmetry functions. NNP4 is shown in red to distinguish it from rest of the NNPs. The $*$ shows the location and energy of the stable stacking fault. All initial structures here are contained in the training dataset, with the non-DFT results corresponding to relaxed structures using the relevant potential.

while the basal core is unstable except at very high temperatures [69]. The EAM potential (Mendelev and Ackland [4] "no. 3") shows the pyramidal I-n to be much higher in energy (24 meV/Å) and also shows a gliding basal core [15] not found in *ab initio* calculations nor observed; the EAM potential is thus not quantitatively accurate. As shown in Fig. 9, the NNP4 predicts two stable core structures at T = 0 K, one on the prismatic I-w plane and one on the pyramidal I-n plane. The first core structure is very compact and the glide plane direction is hard to distinguish via the Nye tensor field. However, the differential displacement maps (see Fig. 9) and disregistry gradients show disassociation on the prismatic I-w plane. Under a small resolved shear stress, this dislocation also glides along the prismatic plane. This prismatic I-w core remains stable when heated to 100 K with molecular dynamics evolution. Furthermore, the edge components of the Nye tensor are almost negligible for this core, which can only be the case for the prismatic I-w $\langle \mathbf{a} \rangle$ due to symmetry requirements.

The second core is on the pyramidal I-n plane and is found to be metastable, transforming to the prismatic I-w core during molecular dynamics at 100 K. Using the NNP for the DFT structures of Ref. [72] (192 atom periodic cells with dislocation dipoles), we compute a pyramidal I-n energy that is 3.8 meV/Å higher than the prismatic I-w energy, in very good agreement with the DFT. Furthermore, the NNP then enables study of the same dislocations in much larger simulation cells, thus eliminating spurious energy contributions that arise when using the small periodic dipolar cells. In large cells (14 976 atoms or more), the NNP predicts that the energy difference between the pyramidal I-n and prismatic I-w dislocations increases to 7 meV/Å, independent of cell size. The NNP thus both captures the DFT results and enables a more-realistic energy difference to be determined, which will lead to accurate modeling of the stresses and temperatures needed to activate any pyramidal I-n $\langle \mathbf{a} \rangle$ slip. No stable dislocation on the basal plane was found, using a number of different initial

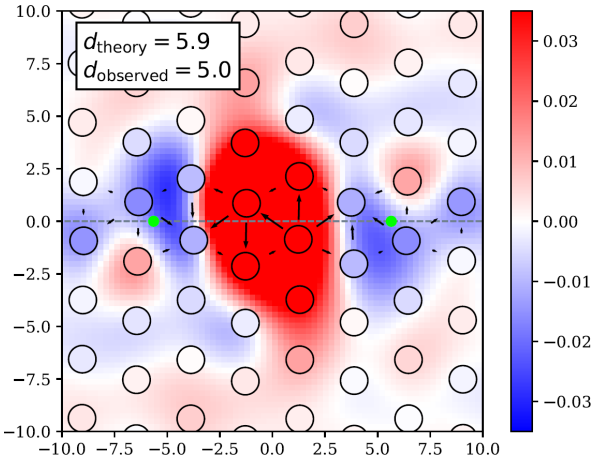

(a) Prismatic I-w plane

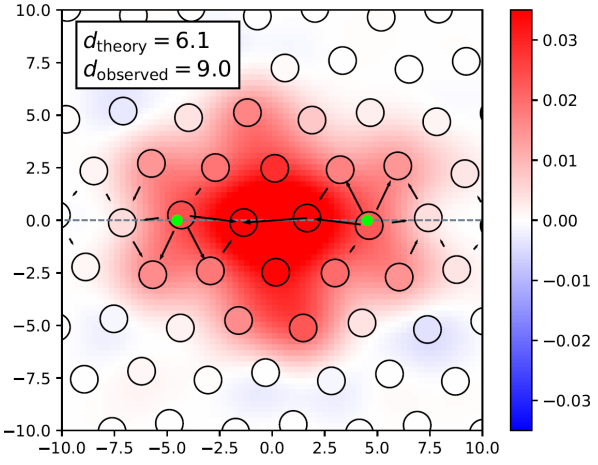

(b) Pyramidal I-n plane

FIG. 9. Atomistic core structures for the $\langle \mathbf{a} \rangle$ screw dislocation in the prismatic I-w and pyramidal I-n planes with the Nye tensor screw components and differential displacement maps overlaid. Green circles indicate the centers of the partial dislocations as identified by the disregistry plots. Theoretical and observed dislocation separation distances are indicated as d_{theory} and d_{observed} (in Å), respectively. These structures are not contained in the training dataset.

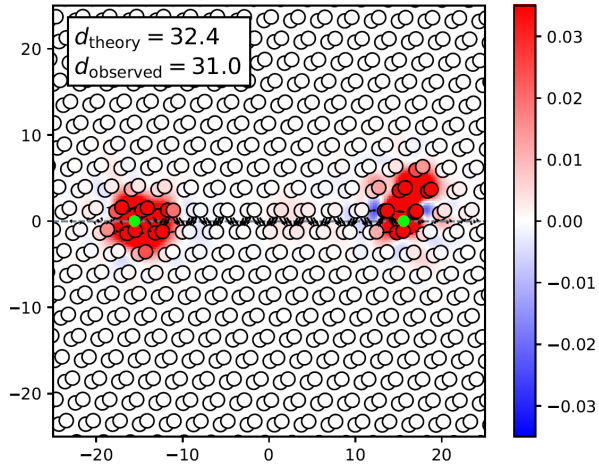

(a) Pyramidal I-w plane

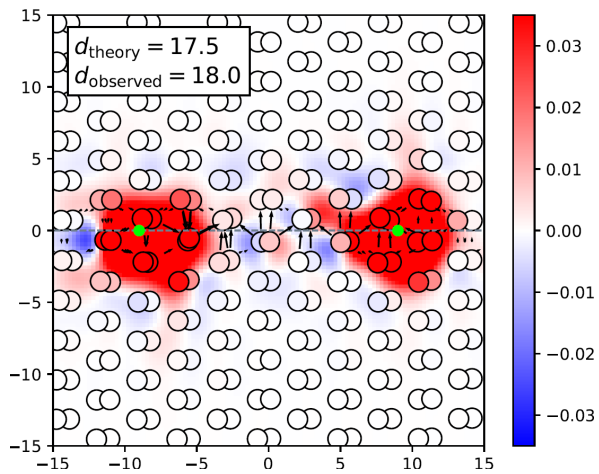

(b) Pyramidal II plane

FIG. 10. Atomistic core structures for the $\langle \mathbf{c} + \mathbf{a} \rangle$ screw dislocation in the pyramidal I-w and pyramidal II planes with the Nye tensor screw components and differential displacement maps overlaid. Green circles indicate the centers of the partial dislocations as identified by the disregistry plots. Theoretical and observed dislocation separation distances are indicated as d_{theory} and d_{observed} (in Å), respectively. These structures are not contained in the training dataset.

conditions to attempt to find a stable configuration. The NNP4 thus predicts all of the observed behaviors found in Zr, and with very good quantitative accuracy in the energy difference relative to the DFT result computed using different details. This represents a significant success for the Zr NNP4 and is a notable improvement over the predictions of any other potentials.

Deformations in the *c*-axis direction of Zr are found to be facilitated through twinning and $\langle \mathbf{c} + \mathbf{a} \rangle$ dislocations that are shared by both the pyramidal I-w and pyramidal II planes (see Fig. 1). The experimental consensus is that $\langle \mathbf{c} + \mathbf{a} \rangle$ glide occurs along the pyramidal I-w plane [73–79] and not the pyramidal II plane. Only Long *et al.* [78] observed a dislocation with pyramidal II glide, but this result is suspected to be due to the presence of Nb [79]. The NNP4 predicts a stable $\langle \mathbf{c} + \mathbf{a} \rangle$ screw dislocation on the pyramidal I-w plane. A metastable pyramidal II dislocation core is also observed with an energy 64 meV/Å higher (see Fig. 10). This is a very large energy difference, indicating strong preference for the pyramidal I-w plane. Hence, when a Burgers-vector-length pyramidal II screw is studied in molecular dynamics at 100 K, it quickly cross-slips into the more stable pyramidal I-w structure.

In contrast, available EAM potentials did not consider the stable stacking fault energies of the pyramidal planes. The resulting values for both the energy and the minimum position are thus inaccurate relative to DFT. Hence, the EAM potentials are likely not suitable for modeling $\langle \mathbf{c} + \mathbf{a} \rangle$ dislocations.

Compared to screw dislocations, edge dislocations can be uniquely defined for each of slip system. NNP4 predicts reasonable core structures for most of the edge dislocations in hcp Zr. Figure 11 shows the edge and screw components of the

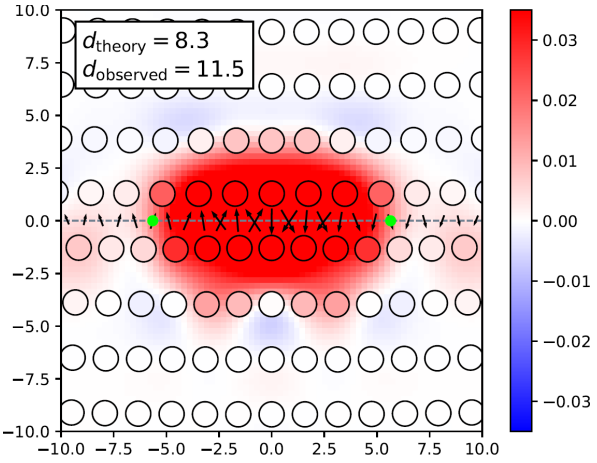

(a) Edge component

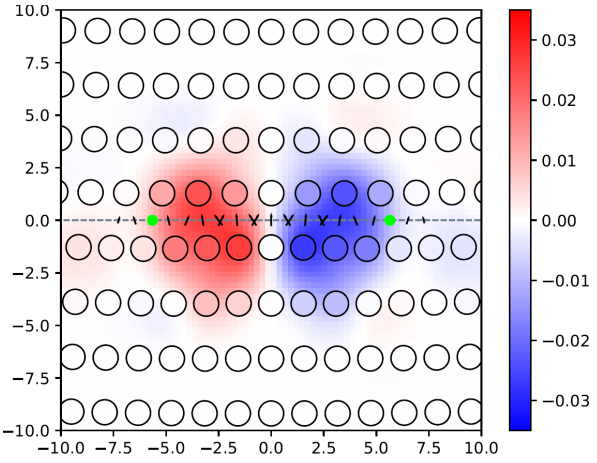

(b) Screw component

FIG. 11. Atomistic core structures for the ⟨**a**⟩ edge dislocation in the basal plane with the Nye tensor and differential displacement maps overlaid. Green circles indicate the centers of the partial dislocations as identified by the disregistry plots. Theoretical and observed dislocation separation distances are indicated as d_{theory} and d_{observed} (in Å), respectively. These structures are not contained in the training dataset.

Nye tensor of the ⟨**a**⟩ edge dislocation along the basal plane. The ⟨**a**⟩ $(1/3\langle 1\bar{2}10\rangle)$ dislocation disassociates into mixed partial dislocations $(1/3[1\bar{1}00]$ and $1/3[0\bar{1}10])$ as expected. Similarly, ⟨**a**⟩ edge dislocations on the prismatic I-w and pyramidal I-n slip planes disassociate into partial dislocations with Burgers vectors corresponding to the positions of the stable stacking faults.

For the ⟨**c** + **a**⟩ edge dislocation, the slip system in pyramidal I-w plane is modeled without any issues. For slip along the pyramidal II plane, however, two core arrangement are observed (see Fig. 12) differing in energy by 6.04 meV/Å. The lower-energy structure shows a local rearrangement (shown with the yellow square in Fig. 12(a)) close to one of the partial dislocations. This is expected to be an artifact of the potential and disappears when the spacing between the partials is increased. The rearrangement can be identified as

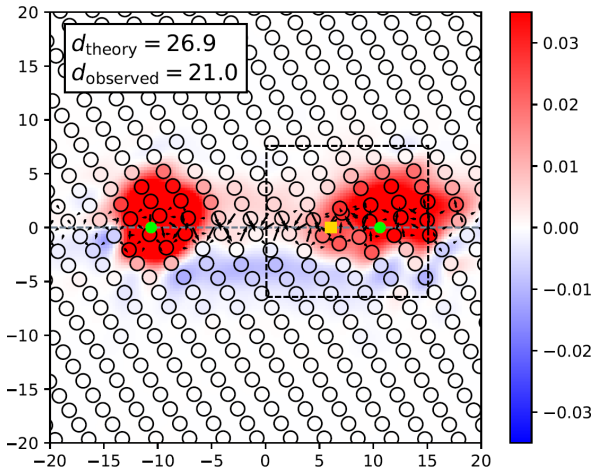

(a) With the local rearrangement

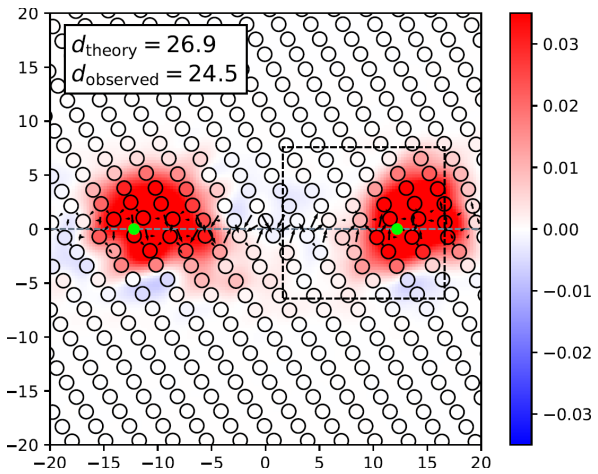

(b) Without any arrangement

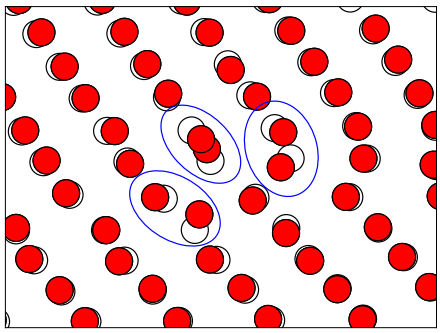

(c) Rearrangement of atoms

FIG. 12. The two atomistic core structures for the ⟨**c** + **a**⟩ edge dislocation in the pyramidal II plane with the Nye tensor and differential displacement maps overlaid, with green circles indicating the centers of the partial dislocations as identified by the disregistry plots. Theoretical and observed dislocation separation distances are indicated as d_{theory} and d_{observed} (in Å), respectively. The yellow square shows the location of the spurious local rearrangement in structure (a). In (c) this region is magnified and overlapped with the same region in structure (b), with red atoms showing structure in (a) and white atoms showing structure in (b). These structures are not contained in the training dataset.

mainly associated with three atom pairs, as seen in Fig. 12(c) (contained in blue ovals), where the red atoms shows the low energy structure with the artifact and the white atoms show the structure without the artifact. The higher energy structure in Fig. 12(b) is more likely to be the physical core structure. However, as observed in previous studies, pyramidal II dislocations are rarely observed. These dislocations might only be created in a specific fracture geometry along the basal plane (see Sec. III F). Hence, this artifact is not expected to be a significant issue in modeling any plastic behavior in Zr.

As a further qualitative examination of the dislocation structures, the partial dislocation distance d is estimated within anisotropic elasticity theory as

$$d_{\text{theory}} = \frac{\mathbf{b}_i^{(1)}\mathbf{K}_{ij}\mathbf{b}_j^{(2)}}{2\pi\gamma_{\text{ssf}}}, \tag{11}$$

where $\mathbf{b}^{(1)}$ and $\mathbf{b}^{(1)}$ are the Burgers vectors of the partial dislocations, $\mathbf{K}$ is the Stroh matrix [80,81], and γ_{ssf} is the stable stacking fault energy of the respective plane. Figures 9–12 indicate the analytically estimated (d_{theory}) and atomistically observed (d_{observed} obtained using gradients of the atomistic disregistry across the slip plane) partial spacing for several core structures. NNP4 shows general agreement, providing further confidence in the potential. Significant deviations that would point to possible subtle problems in a potential are not found.

As mentioned above, the stacking faults of the EAM potential (Mendelev and Ackland [4] "no. 3") vary rather significantly from the DFT properties, hinting at challenges in modeling dislocations. The EAM can give some adequate core structures but several shortcomings are also observed. The $\langle\mathbf{a}\rangle$ screw dislocation shows a stable basal structure that should not exist (see also Clouet [15]). In addition, the partial separation distances can vary more significantly from the elasticity estimate mainly for the $\langle\mathbf{c}+\mathbf{a}\rangle$ dislocations.

E. Twin boundaries

Plastic deformation in hcp Zr is mainly accommodated by the prismatic $\langle\mathbf{a}\rangle$ dislocations. Generalized plasticity requires, however, c-axis deformation, which is achieved in Zr by either pyramidal I-w $\langle\mathbf{c}+\mathbf{a}\rangle$ dislocations or twinning [70,76,82,83]. Twinning is observed abundantly at low temperatures (twinning almost exclusively contributes to c-axis deformation below 77 K [76,84]) and high strain rates, while $\langle\mathbf{c}+\mathbf{a}\rangle$ dislocations become dominant at high temperatures (above 373 K slip dominates the deformation). Four different twin systems have been observed in Zr. For tensile strains (extensions) along the c axis, $\{10\bar{1}2\}$ (T-I) twins are most frequently observed while $\{11\bar{2}1\}$ (T-II) twins are increasingly observed at high strain rates and temperatures [70,76,85]. For compressive strains (contraction) along the c axis, the $\{11\bar{2}2\}$ (C-I) twins are predominantly observed with the $\{10\bar{1}1\}$ (C-II) observed only at high temperatures [85].

The NNP development here contained no twin boundaries in the training set. Thus the ability of NNP4 to predict the structures and energies of the four observed twinning systems is examined. Simulation cells containing twin boundaries were created, with periodicity along the twin planes. Boundaries above and below the twin plane at a distance of ~300 Å were free, and all atoms were relaxed to the low-energy stable structures. The minimum energy structures are shown in Fig. 13 and agree well with those obtained by DFT Mackain *et al.* [83]. The predicted twin boundary energies also agree very well with DFT, as shown in Table II. NNP4 correctly reproduces the relative energies across the four boundaries, and also the very low energy of the C-II boundary. In contrast, predictions using the EAM potential (Mackain *et al.* [83]) show an accurate energy for the T-I boundary but errors of 35%–60% for all others. Without any training information,

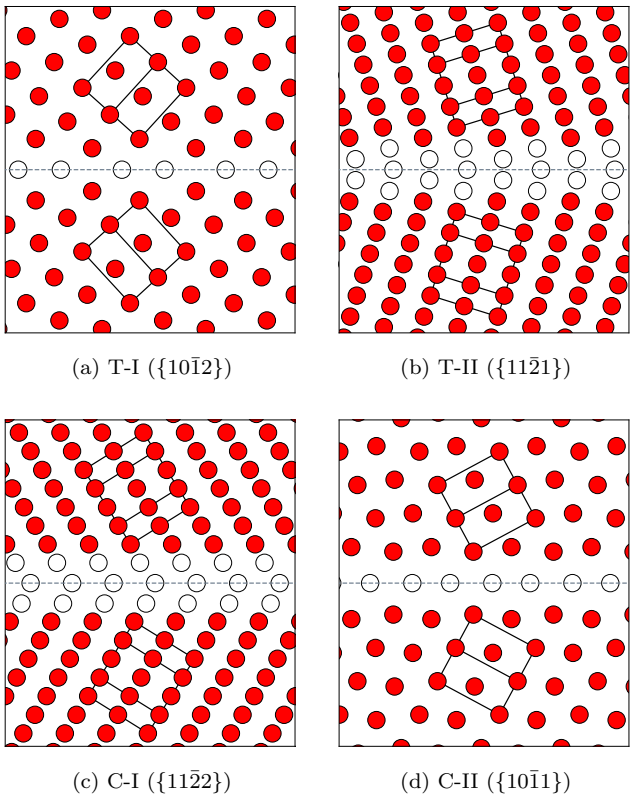

(a) T-I ($\{10\bar{1}2\}$) (b) T-II ($\{11\bar{2}1\}$)

(c) C-I ($\{11\bar{2}2\}$) (d) C-II ($\{10\bar{1}1\}$)

FIG. 13. Relaxed twin boundaries obtained with the NNP4 potential relevant for the deformation twins observed for Zr. Red circles represent atoms in hcp crystal structures, and white circles represent atoms which cannot be classified to any structural system as identified by common neighbor analysis [86,87]. Twin boundaries are shown with a dashed line, and an outline of the orthogonal unit cell for hcp Zr is shown on either side of the twin boundary. These structures are not contained in the training dataset.

TABLE II. Twin boundary energies (in mJ/m^2) as predicted by NNP4 potential and as computed by DFT [83] and [88]. These structures are not contained in the training dataset.

System	NNP4	DFT[a]	DFT[b]
T-I	270	272	253
T-II	211	229	—
C-I	290	355	—
C-II	94	96	65

[a]Mackain *et al.* [83].
[b]Kumar *et al.* [88].

NNP4 thus captures the twin boundary structures and energies extremely well, and notably outperforms the EAM potential.

F. Fracture

Fracture is perhaps the most difficult phenomenon to model due to the complex behavior involving high stresses at the tip of an atomistically sharp crack. Semi-infinite cracks, which are the key reference structures to obtain the relevant critical stress intensity factors for various behaviors, are not periodic. Thus, DFT calculations of fracture are challenging, and require the use of short center cracks in small system sizes, then requiring very high applied loads at which the entire sample is deforming nonlinearly (see Andric and Curtin [89]). Many empirical potentials also fail to show physically reasonable behavior near the crack tip, and across various metals and crystal structures (fcc, bcc, hcp). However, capturing the correct crack tip behavior is quite important since it determines whether a material is intrinsically ductile or brittle. More broadly, no problems involving the creation or evolution of cracks can be studied using a potential that fails for the sharp crack.

The relevant quantities controlling fracture behavior are the three stress intensity factors K_I, K_{II}, and K_{III} for opening, in-plane shearing, and antiplane shearing, respectively, that uniquely characterize the asymptotic singular fields around a crack, independent of the overall problem geometry or applied loads. Of most interest is the mode I opening behavior, for which there are two fundamental crack tip responses: brittle cleavage that maintains a sharp crack occurring at the critical value K_{Ic} [90] and dislocation emission that blunts the crack and encourages ductility occurring at the critical value K_{Ie} [91,92]. These two critical quantities depend on the surface energy γ_s and unstable stacking fault energy γ_{usf} for the relevant cleavage and fracture planes. Linear elastic fracture mechanics predicts that the critical values are

$$K_{Ic} = \sqrt{\frac{2\gamma_s}{\Lambda_{22}}}, \tag{12}$$

$$K_{Ie} = \frac{\sqrt{G_{Ie}\, o(\theta,\phi)}}{|F_{12}(\theta)|}, \tag{13}$$

with

$$G_{Ie} = \begin{cases} 0.145\gamma_s + 0.5\gamma_{\text{usf}} & \gamma_s > 3.45\gamma_{\text{usf}} \\ \gamma_{\text{usf}} & \gamma_s < 3.45\gamma_{\text{usf}} \end{cases}, \tag{14}$$

where Λ_{22} and $o(\theta,\phi)$ are anisotropic elastic constant factors, θ is the inclination of slip plane relative to the crack plane, ϕ is the the orientation angle of the dislocation Burgers vector relative to the crack front direction in the slip plane, and $F_{12}(\theta)$ is a geometric factor related to the angular distribution of shear stress at the crack tip. In simulations with an increasing applied K, the controlling behavior (cleavage or emission) is determined by the smaller of K_{Ic} and K_{Ie}. These predictions are not exact and so should be considered as indicative rather than definitive. Also, although these criteria depend only on basic material properties that are often fit in the development of an interatomic potential, capturing these values accurately in no way ensures that an actual simulation of the crack tip fracture behavior will be physical.

Fracture is studied using the K-controlled geometry in a cell with in-plane dimensions ~300 Å× 300 Å and minimum periodicity along the crack front [89]. Loading is accomplished by displacing all atoms according to the anisotropic elastic solution at an initial stress intensity factor slightly below the theoretically predicted controlling value (K_{Ic} or K_{Ie}). Atoms near the boundary are held fixed and then all interior atoms are relaxed to equilibrium. Displacements are then incremented by a small ΔK followed by full relaxation of the interior atoms, and the response monitored for crack tip behavior (cleavage, emission, or other behavior). To avoid crack closure below K_{Ic}, atomic interactions between atoms on either side of the crack plane are set to zero. Five different crack systems (crack plane, crack front direction) are studied: basal I $\{0001\}\langle 1\bar{2}10\rangle$, basal II $\{0001\}\langle 10\bar{1}0\rangle$, prismatic I $\{10\bar{1}0\}\langle 1\bar{2}10\rangle$, pyramidal I $\{10\bar{1}1\}\langle 1\bar{2}10\rangle$, and pyramidal II $\{11\bar{2}1\}\langle 10\bar{1}0\rangle$.

Initial NNPs trained without the cuboidal and rod structures are found to show nonphysical behavior near crack tips (e.g., amorphization.). Such behavior was previously seen in studies on Mg and other systems. All results in this paper are based on training that included these addition structures, which were found to successfully resolve issues in the fracture behavior of Mg.

Atomistic simulations using the NNP4 potential show one of the two expected mechanism (brittle cleavage, ductile emission) and at K levels comparable to the theoretical values predicted using the NNP4 properties (see Table III) for all crack geometries studied. Figure 14 shows atomistic images of the system just after the creation of the failure event. In general, all the cracks are well behaved and nearly all show no spurious deformations. The main problematic case is the basal II system, where at failure there is some disordering close to the crack tip. This disorder [see Fig. 14(b)] appears similar to the artifacts observed in the pyramidal II dislocation edge core structure, which is the dislocation that is predicted to be emitted from this crack geometry. Cleavage is the predicted failure mechanism but the difference in critical K value between cleavage and emission is very small and cleavage can be hindered by lattice trapping [93]. So, emission is not surprising. Another deviation from theory is that the mechanism operative for the pyramidal I crack plane is observed to be cleavage but emission is predicted because K_{Ic} is ~10% higher than K_{Ie}. This is a notable difference which, since the K value is close to K_{Ic} suggests that emission is being inhibited in this geometry. The critical loads in other cases are quite close to the predicted values.

Table III also shows the predicted critical K_I values using the DFT material properties. Fracture calculations were not performed with DFT as the system sizes required are too large to perform DFT calculations. The values differ slightly from those obtained with the NNP4 potential. However, with these small differences, the predicted mechanisms can be different in a few cases. For the basal I case, DFT predicts cleavage and emission to be equal while the NNP predicts emission. Hence, the NNP may overestimate stability of basal I cracks, and real Zr may be more prone to cleavage. Basal II, prismatic I-w, and pyramidal I-w are all predicted to show the same phenomenon in DFT and NNP4. DFT values predict that pyramidal II should show cleavage, while NNP4 predicts emission, which

TABLE III. Comparison of predicted and simulation fracture behavior (load level and event) for sharp cracks using the NNP4 potential. The theoretical critical stress intensity factor $K_{\mathrm{I,theo}}$ is the smaller of K_{Ic} and K_{Ie} and is shown in bold. The stress intensity factor at failure as found in the simulations is denoted as $K_{\mathrm{I,sim}}$. Predictions using DFT material properties are shown for comparison.

		Prediction			Simulation	
Orientation		K_{Ic}	K_{Ie}	Event	Event	$K_{\mathrm{I,sim}}/K_{\mathrm{I,theo}}$
Basal I	NNP4	0.588	**0.558**	Emit-Pyramidal	Emit-Pyramidal	0.954
	DFT	**0.587**	**0.587**	Emit/Cleave		
Basal II	NNP4	**0.588**	0.598	Cleave	Disordering+emission	1.018
	DFT	**0.587**	0.654	Cleave		
Prismatic I-w	NNP4	0.569	**0.548**	Emit-Basal	Emit-Basal	1.020
	DFT	0.599	**0.577**	Emit-Basal		
Pyramidal I-w	NNP4	0.566	**0.518**	Emit-Basal	Cleave	1.094
	DFT	0.584	**0.545**	Emit-Basal		
Pyramidal II	NNP4	0.593	**0.579**	Emit-Basal	Emit-Basal	0.986
	DFT	**0.609**	0.615	Cleave		

is observed in the simulations. All of these competitions are very subtle, and the true behavior can differ from the DFT estimate. Hence, we mainly look for consistency and avoidance of unphysical crack tip behavior. Finally, the crack tip behavior observed for other NNPs having the same set of symmetry functions as NNP4 give similar results for fracture, so that NNP4 is not special in this regard.

The EAM potential (Mendelev and Ackland [4] "no. 3") shows reasonable predictions for surface energies but not for unstable stacking fault energies. Hence, the EAM is not expected to predict fracture behavior accurately. Indeed, the EAM potential shows mainly cleavage failure in simulations, contradicting almost all predictions based on DFT and EAM properties. The cleavage failure also displayed unusual behavior where the crack extension was gradual with increasing stress, whereas the crack should normally extend further when K_{Ic} is reached. These variations could be due to the limitations in the properties used when fitting the EAM. Properties such

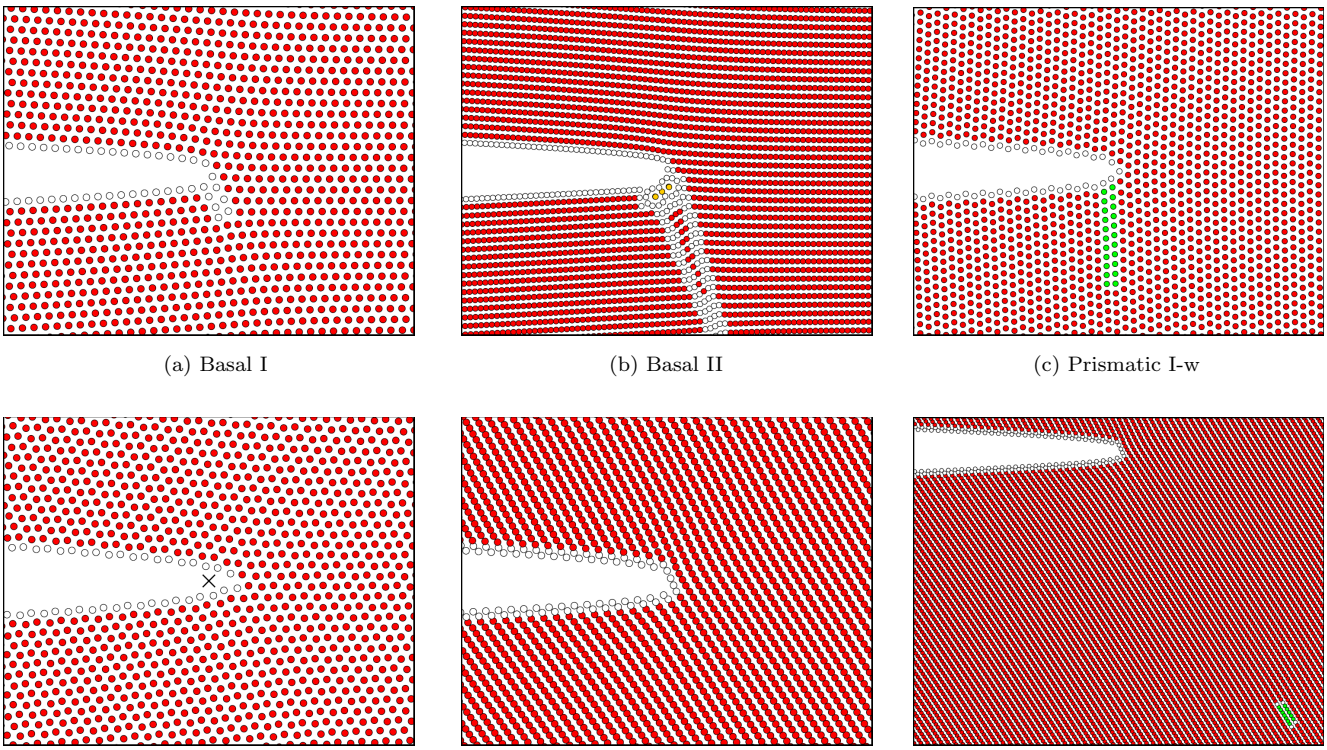

(a) Basal I (b) Basal II (c) Prismatic I-w

(d) Pyramidal I-w (e) Pyramidal II - near tip (f) Pyramidal II - emitted dislocation

FIG. 14. Postfracture view of the near crack tip region for sharp crack tips obtained with the NNP4 potential, where red, green, and yellow circles represent atoms in hcp, fcc, and icosahedral crystal structures, respectively, and white circles represent atoms which cannot be classified to any structural system as identified by common neighbor analysis [86,87]. For the pyramidal I system, the initial crack tip location is shown with a "×". These structures are not contained in the training dataset.

as surface energies and stacking fault energies that are important for fracture behavior, are not considered adequately. Hence the behavior around crack tips may not be properly captured with the EAM.

IV. CONCLUSION

A neural network potential (NNP) has been developed for hcp Zr that achieves the goal of providing a broadly accurate potential for a wide range of applications. This Behler-Parrinello NNP is constructed based on previous NNP development experience for metals and alloys. It is found necessary to greatly expand the number and nature of the symmetry functions, relative to those used in hcp Mg and fcc Al-based alloys. The c/a ratio differs substantially from the ideal value, unlike in Mg, and thus creating many more complex local environments within the typical structures. This makes the requirement for symmetry functions capturing the angular relationships higher, thereby increasing an expansion of the total symmetry functions. In particular, it is found necessary to include wide angular symmetry functions and use a radial cutoff of 7.0 Å to obtain an accurate description of some key Zr properties.

The selected NNP, labeled NNP4, shows very good agreement for mechanical properties, GSFE curves, stable stacking fault energies, decohesion curves, and surface energies, across the spectrum of slip and fracture planes relevant for deformation and fracture. Beyond matching the properties coming directly from DFT energies, NNP4 shows very good twin boundaries, dislocation structures, and fracture behavior. One notable success is the correct prediction of the relative energetics of the $\langle \mathbf{a} \rangle$ screw, with the prismatic plane slightly

TABLE IV. Hyperparameters for the symmetry functions as described in Eqs. (2)– (4), where type 2, type 3, and type 9 are for radial (G^2), narrow angular (G^3), and wide angular (G^9) symmetry functions, respectively. $r_c = 7.0$ for all the symmetry functions.

Type	η	λ	ζ	r_s	Type	η	λ	ζ	r_s
2	2.000	–	–	0.50	3	5.102×10^{-1}	−1	1	–
2	2.000	–	–	3.50	3	5.102×10^{-1}	1	1	–
2	2.000	–	–	4.00	3	5.102×10^{-1}	−1	3	–
2	2.000	–	–	4.50	3	5.102×10^{-1}	1	3	–
2	2.000	–	–	5.00	3	5.102×10^{-1}	−1	12	–
2	2.000	–	–	5.50	3	5.102×10^{-1}	1	12	–
2	2.000	–	–	6.00	3	5.102×10^{-1}	−1	64	–
2	2.000	–	–	6.50	3	5.102×10^{-1}	1	64	–
2	2.041×10^{-2}	–	–	0.00	9	2.041×10^{-2}	−1	1	–
2	3.885×10^{-2}	–	–	0.00	9	2.041×10^{-2}	−1	3	–
2	7.396×10^{-2}	–	–	0.00	9	2.041×10^{-2}	1	3	–
2	1.408×10^{-1}	–	–	0.00	9	2.041×10^{-2}	−1	12	–
2	2.680×10^{-1}	–	–	0.00	9	2.041×10^{-2}	1	12	–
2	5.102×10^{-1}	–	–	0.00	9	2.041×10^{-2}	−1	64	–
3	2.041×10^{-2}	1	1	–	9	2.041×10^{-2}	1	64	–
3	2.041×10^{-2}	−1	3	–	9	7.396×10^{-2}	1	1	–
3	2.041×10^{-2}	−1	12	–	9	7.396×10^{-2}	−1	3	–
3	2.041×10^{-2}	1	12	–	9	7.396×10^{-2}	−1	12	–
3	2.041×10^{-2}	−1	64	–	9	7.396×10^{-2}	1	12	–
3	3.885×10^{-2}	−1	12	–	9	7.396×10^{-2}	−1	64	–
3	3.885×10^{-2}	−1	64	–	9	7.396×10^{-2}	1	64	–
3	3.885×10^{-2}	1	64	–	9	1.408×10^{-1}	−1	1	–
3	7.396×10^{-2}	1	1	–	9	1.408×10^{-1}	−1	3	–
3	7.396×10^{-2}	−1	3	–	9	1.408×10^{-1}	1	3	–
3	7.396×10^{-2}	1	12	–	9	1.408×10^{-1}	−1	12	–
3	7.396×10^{-2}	−1	64	–	9	1.408×10^{-1}	1	12	–
3	7.396×10^{-2}	1	64	–	9	1.408×10^{-1}	−1	64	–
3	1.408×10^{-1}	1	1	–	9	1.408×10^{-1}	1	64	–
3	1.408×10^{-1}	−1	3	–	9	2.680×10^{-1}	−1	3	–
3	1.408×10^{-1}	−1	12	–	9	2.680×10^{-1}	1	3	–
3	1.408×10^{-1}	1	12	–	9	2.680×10^{-1}	−1	12	–
3	1.408×10^{-1}	−1	64	–	9	2.680×10^{-1}	1	12	–
3	1.408×10^{-1}	1	64	–	9	2.680×10^{-1}	−1	64	–
3	2.680×10^{-1}	1	1	–	9	2.680×10^{-1}	1	64	–
3	2.680×10^{-1}	−1	3	–	9	5.102×10^{-1}	1	1	–
3	2.680×10^{-1}	−1	12	–	9	5.102×10^{-1}	−1	3	–
3	2.680×10^{-1}	1	12	–	9	5.102×10^{-1}	1	3	–
3	2.680×10^{-1}	−1	64	–	9	5.102×10^{-1}	−1	12	–
3	2.680×10^{-1}	1	64	–	9	5.102×10^{-1}	1	12	–

favored over the pyramidal I plane and the basal plane showing no stable structure. Another notable success is the accurate predictions of the structures and energies of all four twin systems, none of which were included in the training set.

Several issues remain to be rectified in future generations of a machine learning potential for hcp Zr. First, the behavior in high compression is poor because this domain is outside the scope of the training set. The unphysical behavior can be rectified by the ad-hoc addition of a repulsive potential (see Fig. 6) but this is not a full solution. Expanding the training data is possible, but the addition of high-energy structures could drive the NNP toward fitting of those structures at the expense of lower-energy structures related to more-crucial properties. Other regression methods using the current training set or an expanded training set might show better results. Lastly, the pyramidal II edge dislocation core shows some likely unphysical local rearrangements in the lowest-energy structure. Fortunately, pyramidal II slip is not very relevant in Zr, since pyramidal I-w slip dominates. But this rearrangement does affect the crack tip behavior of the basal II orientation where emission onto the pyramidal II plane should occur, and so improvements to the pyramidal II slip description remain desirable.

In spite of some of the above limitations, comparisons of NNP4 against the EAM potential (Mendelev and Ackland [4] "no. 3") show that NNP4 is clearly superior. NNP4 not only predicts basic properties as well or better than the EAM potential, but is far better in capturing intricate details related to dislocations, twins, and fracture. Other EAM potentials not discussed here were also studied and showed even poorer performance than the EAM potential (Mendelev and Ackland [4] "no. 3"). While the computational cost of NNP4 is approximately one order of magnitude higher than that for the EAM potential, the far better accuracy in qualitative and quantitative predictions related to metallurgical phenomena fully offsets the increased computational cost.

In light of our present study, the current NNP4, while not perfect, sets a standard for the performance of interatomic Zr potentials. Future work will involve extending this NNP framework to Zr-H and Zr alloys. This will enable accurate simulations of critical application problems of Zr alloys in nuclear reactors.

ACKNOWLEDGMENTS

We thank J. Wormald of the US Naval Nuclear Laboratory and the colleagues at Materials Design, especially J.-R. Hill and E. Wimmer, for helpful discussions about this work. This work was funded by the Advanced Materials Simulation Engineering Tool (AMSET) project, sponsored by the Naval Nuclear Laboratory and directed by Materials Design, Inc. W.A.C. also thanks the NCCR MARVEL, a National Centre of Competence in Research, funded by the Swiss National Science Foundation (Grant No. 182892) for support of this work.

APPENDIX: SYMMETRY FUNCTION HYPERPARAMETERS USED IN DEVELOPING NNP4 POTENTIAL

Hyperparameters of the symmetry functions used when developing the NNP4 potential are shown in Table IV. Symmetry function types 2, 3, and 9 corresponds to G^2, G^3, and G^9 symmetry functions as shown in Eqs. (2)– (4), respectively.

[1] R. Krishnan and M. K. Asundi, Zirconium alloys in nuclear technology, in *Proceedings of the Indian Academy of Sciences Section C: Engineering Sciences*, vol. 4 (Springer, Berlin, 1981), pp. 41–56

[2] J. A. L. Robertson, Zirconium—An international nuclear material, J. Nucl. Mater. **100**, 108 (1981).

[3] S. Banerjee, Nuclear applications: Zirconium alloys, in *Encyclopedia of Materials: Science and Technology*, edited by K. J. Buschow, R. W. Cahn, M. C. Flemings, B. Ilschner, E. J. Kramer, S. Mahajan, and P. Veyssière (Elsevier, Oxford, 2001), pp. 6287–6299

[4] M. I. Mendelev and G. J. Ackland, Development of an interatomic potential for the simulation of phase transformations in zirconium, Philos. Mag. Lett. **87**, 349 (2007).

[5] D. O. Northwood, The development and applications of zirconium alloys, Mater. Des. **6**, 58 (1985).

[6] M. S. Blackmur, J. D. Robson, M. Preuss, O. Zanellato, R. J. Cernik, S.-Q. Shi, F. Ribeiro, and J. Andrieux, Zirconium hydride precipitation kinetics in zircaloy-4 observed with synchrotron x-ray diffraction, J. Nucl. Mater. **464**, 160 (2015).

[7] E. Chajduk and A. Bojanowska-Czajka, Corrosion mitigation in coolant systems in nuclear power plants, Prog. Nucl. Energy **88**, 1 (2016).

[8] R. J. McCabe, G. Proust, E. K. Cerreta, and A. Misra, Quantitative analysis of deformation twinning in zirconium, Int. J. Plast. **25**, 454 (2009).

[9] L. Jaworska, J. Cyboron, S. Cygan, A. Zwolinski, B. Onderka, and T. Skrzekut, Zirconium phase transformation under static high pressure and ω-Zr phase stability at high temperatures, Materials **12**, 2244 (2019).

[10] M. Arul Kumar, N. Hilairet, R. J. McCabe, T. Yu, Y. Wang, I. J. Beyerlein, and C. N. Tomé, Role of twinning on the omega-phase transformation and stability in zirconium, Acta Mater. **185**, 211 (2020).

[11] M. S. Daw and M. I. Baskes, Semiempirical, Quantum Mechanical Calculation of Hydrogen Embrittlement in Metals, Phys. Rev. Lett. **50**, 1285 (1983).

[12] M. S. Daw and M. I. Baskes, Embedded-atom method: Derivation and application to impurities, surfaces, and other defects in metals, Phys. Rev. B **29**, 6443 (1984).

[13] M. I. Baskes, Modified embedded-atom potentials for cubic materials and impurities, Phys. Rev. B **46**, 2727 (1992).

[14] B. Yin, Z. Wu, and W. Curtin, Comprehensive first-principles study of stable stacking faults in hcp metals, Acta Mater. **123**, 223 (2017).

[15] E. Clouet, Screw dislocation in zirconium: An *ab initio* study, Phys. Rev. B **86**, 144104 (2012).

[16] N. Chaari, E. Clouet, and D. Rodney, First order pyramidal slip of $1/3\langle 12\bar{1}0\rangle$ screw dislocations in zirconium, Metall. Mater. Trans. A **45**, 5898 (2014).

[17] T. Obara, H. Yoshinga, and S. Morozumi, $\{1122\}\langle 1123\rangle$ slip system in magnesium, Acta Metall. **21**, 845 (1973).

[18] K. Fukuda, Y. Koyanagi, M. Tsushida, H. Kitahara, T. Mayama, and S. Ando, Activation stress for slip systems of pure magnesium single crystals in pure shear test, Mater. Trans. **58**, 587 (2017).

[19] M. Stricker and W. A. Curtin, Prismatic slip in magnesium, J. Phys. Chem. C **124**, 27230 (2020).

[20] Z.-C. Ma, X.-Z. Tang, Y. Mao, and Y.-F. Guo, The plastic deformation mechanisms of hcp single crystals with different orientations: Molecular dynamics simulations, Materials **14**, 733 (2021).

[21] M. Igarashi, M. Khantha, and V. Vitek, *N*-body interatomic potentials for hexagonal close-packed metals, Philos. Mag. B **63**, 603 (1991).

[22] G. J. Ackland, S. J. Wooding, and D. J. Bacon, Defect, surface and displacement-threshold properties of α-zirconium simulated with a many-body potential, Philos. Mag. A **71**, 553 (1995).

[23] R. C. Pasianot and A. M. Monti, A many body potential for α-Zr. application to defect properties, J. Nucl. Mater. **264**, 198 (1999).

[24] Y.-M. Kim, B.-J. Lee, and M. I. Baskes, Modified embedded-atom method interatomic potentials for Ti and Zr, Phys. Rev. B **74**, 014101 (2006).

[25] E. Wimmer, M. Christensen, W. Wolf, W. H. Howland, B. Kammenzind, and R. W. Smith, Hydrogen in zirconium: Atomistic simulations of diffusion and interaction with defects using a new embedded atom method potential, J. Nucl. Mater. **532**, 152055 (2020).

[26] H. Zong, G. Pilania, X. Ding, G. J. Ackland, and T. Lookman, Developing an interatomic potential for martensitic phase transformations in zirconium by machine learning, npj Comput. Mater. **4**, 48 (2018).

[27] H. Zong, Y. Luo, X. Ding, T. Lookman, and G. J.Ackland, hcp $\rightarrow\omega$ phase transition mechanisms in shocked zirconium: A machine learning based atomic simulation study, Acta Mater. **162**, 126 (2019).

[28] H. Zong, P. He, X. Ding, and G. J. Ackland, Nucleation mechanism for hcp $\rightarrow$ bcc phase transformation in shock-compressed Zr, Phys. Rev. B **101**, 144105 (2020).

[29] P. Liu, C. Verdi, F. Karsai, and G. Kresse, α-β phase transition of zirconium predicted by on-the-fly machine-learned force field, Phys. Rev. Materials **5**, 053804 (2021).

[30] X. Qian and R. Yang, Temperature effect on the phonon dispersion stability of zirconium by machine learning driven atomistic simulations, Phys. Rev. B **98**, 224108 (2018).

[31] D. Marchand, A. Jain, A. Glensk, and W. A. Curtin, Machine learning for metallurgy I. A neural-network potential for Al-Cu, Phys. Rev. Materials **4**, 103601 (2020).

[32] M. Stricker, B. Yin, E. Mak, and W. A. Curtin, Machine learning for metallurgy II. A neural-network potential for magnesium, Phys. Rev. Materials **4**, 103602 (2020).

[33] A. C. P. Jain, D. Marchand, A. Glensk, M. Ceriotti, and W. A. Curtin, Machine learning for metallurgy III: A neural network potential for Al-Mg-Si, Phys. Rev. Materials **5**, 053805 (2021).

[34] J. Behler and M. Parrinello, Generalized Neural-Network Representation of High-Dimensional Potential-Energy Surfaces, Phys. Rev. Lett. **98**, 146401 (2007).

[35] J. Behler, Atom-centered symmetry functions for constructing high-dimensional neural network potentials, J. Chem. Phys. **134**, 074106 (2011).

[36] A. Hamedani, J. Byggmästar, F. Djurabekova, G. Alahyarizadeh, R. Ghaderi, A. Minuchehr, and K. Nordlund, Insights into the primary radiation damage of silicon by a machine learning interatomic potential, Mater. Res. Lett. **8**, 364 (2020).

[37] F. J. Domínguez-Gutiérrez, J. Byggmästar, K. Nordlund, F. Djurabekova, and U. von Toussaint, Computational study of crystal defect formation in mo by a machine learning molecular dynamics potential, Model. Simul. Mater. Sci. Eng. **29**, 055001 (2021).

[38] P. Hohenberg and W. Kohn, Inhomogeneous electron gas, Phys. Rev. **136**, B864 (1964).

[39] W. Kohn and L. J. Sham, Self-consistent equations including exchange and correlation effects, Phys. Rev. **140**, A1133 (1965).

[40] J. P. Perdew, K. Burke, and M. Ernzerhof, Generalized Gradient Approximation Made Simple, Phys. Rev. Lett. **77**, 3865 (1996).

[41] P. E. Blöchl, Projector augmented-wave method, Phys. Rev. B **50**, 17953 (1994).

[42] G. Kresse and J. Furthmüller, Efficient iterative schemes for *ab initio* total-energy calculations using a plane-wave basis set, Phys. Rev. B **54**, 11169 (1996).

[43] G. Kresse and D. Joubert, From ultrasoft pseudopotentials to the projector augmented-wave method, Phys. Rev. B **59**, 1758 (1999).

[44] H. Monkhorst and J. Pack, Special points for Brillouin-zone integrations, Phys. Rev. B **13**, 5188 (1976).

[45] Medea 3.2, Materials Design, Inc., San Diego, CA (2020).

[46] A. P. Bartók, M. C. Payne, R. Kondor, and G. Csányi, Gaussian Approximation Potentials: The Accuracy of Quantum Mechanics, without the Electrons, Phys. Rev. Lett. **104**, 136403 (2010).

[47] A. Singraber, T. Morawietz, J. Behler, and C. Dellago, Parallel multistream training of high-dimensional neural network potentials, J. Chem. Theory Comput. **15**, 3075 (2019).

[48] A. Singraber, J. Behler, and C. Dellago, Library-based *LAMMPS* implementation of high-dimensional neural network potentials, J. Chem. Theory Comput. **15**, 1827 (2019).

[49] G. Imbalzano, A. Anelli, D. Giofré, S. Klees, J. Behler, and M. Ceriotti, Automatic selection of atomic fingerprints and reference configurations for machine-learning potentials, J. Chem. Phys. **148**, 241730 (2018).

[50] M. Gastegger, L. Schwiedrzik, M. Bittermann, F. Berzsenyi, and P. Marquetand, wACSF-weighted atom-centered symmetry functions as descriptors in machine learning potentials, J. Chem. Phys. **148**, 241709 (2018).

[51] S. Plimpton, Fast parallel algorithms for short-range molecular dynamics, J. Comput. Phys. **117**, 1 (1995).

[52] A. Stukowski, Visualization and analysis of atomistic simulation data with OVITO—The open visualization tool, Model. Simul. Mater. Sci. Eng. **18**, 015012 (2010).

[53] J. Goldak, L. T. Lloyd, and C. S. Barrett, Lattice parameters, thermal expansions, and Grüneisen coefficients of zirconium, 4.2 to 1130° K, Phys. Rev. **144**, 478 (1966).

[54] E. S. Fisher and J. Renken, Single-crystal elastic moduli and the hcp → bcc transformation in Ti, Zr, and Hf, Phys. Rev. **135**, A482 (1964).

[55] S. Zhang, X. Zhang, Y. Zhu, S. Zhang, L. Qi, and R. Liu, First-principles investigations on elastic and thermodynamic properties of zirconium under pressure, Comput. Mater. Sci. **61**, 42 (2012).

[56] H. Ikehata, N. Nagasako, T. Furuta, A. Fukumoto, K. Miwa, and T. Saito, First-principles calculations for development of low elastic modulus Ti alloys, Phys. Rev. B **70**, 174113 (2004).

[57] B.-T. Wang, P. Zhang, H.-Y. Liu, W.-D. Li, and P. Zhang, First-principles calculations of phase transition, elastic modulus, and superconductivity under pressure for zirconium, J. Appl. Phys. **109**, 063514 (2011).

[58] Y.-J. Hao, L. Zhang, X.-R. Chen, Y.-H. Li, and H.-L. He, Phase transition and elastic constants of zirconium from first-principles calculations, J. Phys.: Condens. Matter **20**, 235230 (2008).

[59] J. Zheng, H. Zhang, X. Zhou, J. Liang, L. Sheng, and S. Peng, First-principles study of the structural stability and electronic and elastic properties of helium in α-zirconium, Adv. Condens. Matter Phys. **2014**, 929750 (2014).

[60] Y. Udagawa, M. Yamaguchi, H. Abe, N. Sekimura, and T. Fuketa, *Ab initio* study on plane defects in zirconium-hydrogen solid solution and zirconium hydride, Acta Mater. **58**, 3927 (2010).

[61] C. Domain, R. Besson, and A. Legris, Atomic-scale *ab initio* study of the Zr-H system: II. Interaction of H with plane defects and mechanical properties, Acta Mater. **52**, 1495 (2004).

[62] D. J. Bacon and V. Vitek, Atomic-scale modeling of dislocations and related properties in the hexagonal-close-packed metals, Metall. Mater. Trans. A **33**, 721 (2002).

[63] V. Volterra, Sur l'équilibre des corps élastiques multiplement connexes, Ann. Sci. École Norm. Sup. **24**, 401 (1907).

[64] J. F. Nye, Some geometrical relations in dislocated crystals, Acta Metall. **1**, 153 (1953).

[65] C. S. Hartley and Y. Mishin, Characterization and visualization of the lattice misfit associated with dislocation cores, Acta Mater. **53**, 1313 (2005).

[66] V. Vítek, R. C. Perrin, and D. K. Bowen, The core structure of 1/2(111) screw dislocations in bcc crystals, Philos. Mag. **21**, 1049 (1970).

[67] National Institute of Standards and Technology, atomman: Atomistic Manipulation Toolkit, https://www.ctcms.nist.gov/potentials/atomman/.

[68] E. Clouet, *Ab initio* models of dislocations, in *Handbook of Materials Modeling: Methods: Theory and Modeling*, edited by W. Andreoni and S. Yip (Springer International Publishing, Cham, 2020), pp. 1503–1524.

[69] A. Akhtar, Basal slip in zirconium, Acta Metall. **21**, 1 (1973).

[70] V. Tong, E. Wielewski, and B. Britton, Characterisation of slip and twinning in high rate deformed zirconium with electron backscatter diffraction, arXiv:1803.00236.

[71] D. Caillard, M. Rautenberg, and X. Feaugas, Dislocation mechanisms in a zirconium alloy in the high-temperature regime: An *in situ* TEM investigation, Acta Mater. **87**, 283 (2015).

[72] E. Clouet, D. Caillard, N. Chaari, F. Onimus, and D. Rodney, Dislocation locking versus easy glide in titanium and zirconium, Nat. Mater. **14**, 931 (2015).

[73] J. A. Jensen and W. A. Backofen, Deformation and fracture of alpha zirconium alloys, Can. Metall. Q. **11**, 39 (1972).

[74] A. Akhtar, Compression of zirconium single crystals parallel to the c-axis, J. Nucl. Mater. **47**, 79 (1973).

[75] H. Numakura, Y. Minonishi, and M. Koiwa, ⟨1123⟩{1011} slip in zirconium, Philos. Mag. A **63**, 1077 (1991).

[76] R. J. McCabe, E. K. Cerreta, A. Misra, G. C. Kaschner, and C. N. Tomé, Effects of texture, temperature and strain on the deformation modes of zirconium, Philos. Mag. **86**, 3595 (2006).

[77] J. Gong, T. B. Britton, M. A.Cuddihy, F. P. E. Dunne, and A. J. Wilkinson, $\langle a \rangle$ prismatic, $\langle a \rangle$ basal, and $\langle c + a \rangle$ slip strengths of commercially pure Zr by micro-cantilever tests, Acta Mater. **96**, 249 (2015).

[78] F. Long, J. Kacher, Z. Yao, and M. R. Daymond, A tomographic TEM study of tension-compression asymmetry response of pyramidal dislocations in a deformed Zr-2.5Nb alloy, Scr. Mater. **153**, 94 (2018).

[79] T. Soyez, D. Caillard, F. Onimus, and E. Clouet, Mobility of $\langle \mathbf{c} + \mathbf{a} \rangle$ dislocations in zirconium, Acta Mater. **197**, 97 (2020).

[80] A. N. Stroh, Dislocations and cracks in anisotropic elasticity, Philos. Mag. **3**, 625 (1958).

[81] A. N. Stroh, Steady state problems in anisotropic elasticity, J. Math. Phys. **41**, 77 (1962).

[82] M. H. Yoo, Slip, twinning, and fracture in hexagonal close-packed metals, Metall. Mater. Trans. A **12**, 409 (1981).

[83] O. MacKain, M. Cottura, D. Rodney, and E. Clouet, Atomic-scale modeling of twinning disconnections in zirconium, Phys. Rev. B **95**, 134102 (2017).

[84] S. G. Song and G. T. Gray, Influence of temperature and strain rate on slip and twinning behavior of Zr, Metall. Mater. Trans. A **26**, 2665 (1995).

[85] B.-F. Luan, Q. Ye, J.-W. Chen, H.-B. Yu, D.-L. Zhou, and Y.-C. Xin, Deformation twinning and textural evolution of pure zirconium during rolling at low temperature, Trans. Nonferrous Met. Soc. China **23**, 2890 (2013).

[86] J. D. Honeycutt and H. C. Andersen, Molecular dynamics study of melting and freezing of small Lennard-Jones clusters, J. Phys. Chem. **91**, 4950 (1987).

[87] D. Faken and H. Jónsson, Systematic analysis of local atomic structure combined with 3D computer graphics, Comput. Mater. Sci. **2**, 279 (1994).

[88] A. Kumar, J. Wang, and C. Tomé, First-principles study of energy and atomic solubility of twinning-associated boundaries in hexagonal metals, Acta Mater. **85**, 144 (2015).

[89] P. Andric and W. A. Curtin, Atomistic modeling of fracture, Model. Simul. Mater. Sci. Eng. **27**, 013001 (2019).

[90] A. A. Griffith, VI. The phenomena of rupture and flow in solids, Philos. Trans. R. Soc. A **221**, 163 (1921).

[91] J. R. Rice, Dislocation nucleation from a crack tip: An analysis based on the Peierls concept, J. Mech. Phys. Solids **40**, 239 (1992).

[92] P. Andric and W. A. Curtin, New theory for mode I crack-tip dislocation emission, J. Mech. Phys. Solids **106**, 315 (2017).

[93] W. A. Curtin and H. Scher, Analytic Model for Scaling of Breakdown, Phys. Rev. Lett. **67**, 2457 (1991).